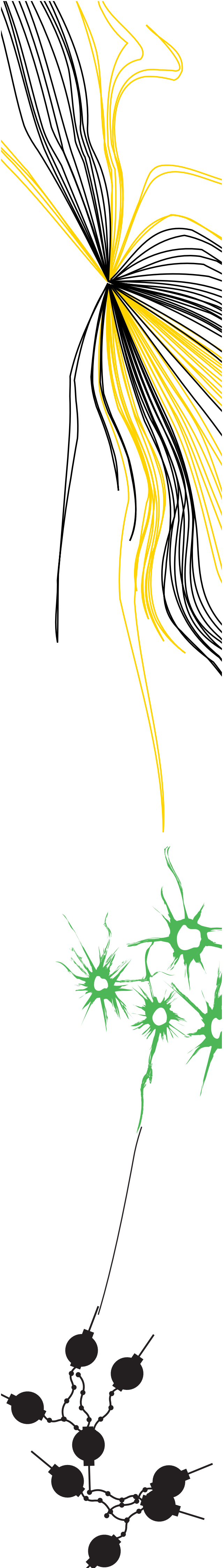

RAM
ROBOTICS
AND
MECHATRONICS

3D PRINTED PIEZO-RESISTIVE FLOW SENSORS FOR USE ON WINGS

J.C (Jiahao) Cui

MSC ASSIGNMENT

Committee:
prof. dr. ir. G.J.M. Krijnen
ir. A.P. Dijkshoorn
dr. ir. A.Q.L. Keemink

March, 2021

010RaM2021
Robotics and Mechatronics
EEMCS
University of Twente
P.O. Box 217
7500 AE Enschede
The Netherlands

UNIVERSITY OF TWENTE. | TECHMED CENTRE
UNIVERSITY OF TWENTE. | DIGITAL SOCIETY INSTITUTE

Summary

At present, the application of 3D printing technology is becoming more and more extensive. In terms of sensors, 3D printing technology also shows great potential. The field of sensor manufacturing based on thermoplastics is our main research direction. The use of such technology to manufacture a flow sensor for a control system is still novel and worth exploring. This research is mainly devoted to use 3D printing technology to make a flow sensor, and exploring its working characteristic in a close-loop control system.

First of all, the first part of this project is the design and printing of the flow sensors. These sensors have piezo-resistive strain gauges which help them to measure the flow. Through mechanical model and dynamic model analysis, several different designs will be tried at the beginning. After printing, the suited model is determined through experiments.

Second, this project experimentally characterize the sensors, both quasi-static for deformations and dynamic for the frequency response. In quasi-static experiment, there is a certain non-linearity and hysteresis between the deformation and the change of resistance of the sensor can be observed. And an approximate linear relationship is obtained. In dynamic experiment, the eigenfrequency of the sensor is obtained.

Next, in order to further explore the relationship between sensor vibration and surrounding airflow, the sensor is placed in the wind tunnel for testing, so that the actual airflow conditions in the experiment can be better known.

Finally, the control system experiment set-up including the drone propeller is designed and built. The control system is close-loop system with PI controller. In this part of the experiment, the working conditions of the sensor in the actual closed-loop control system are studied. The experimental results show that the sensor has under-damping problem, which makes the control system unstable. But a low pass filter with a small cut-off frequency can solve this problem well, so that the control system works normally. Then, more analysis and solution work on this problem are realized in simulation.

Acknowledgements

This report was completed by me in the system and control major. In this thesis research process, many people have given me great help.

First of all, thanks to the two supervisors, Gijs Krijnen and Alexander Dijkshoorn, for their help. Throughout the thesis process, you have provided me with very valuable advice and guidance.

Secondly, I would like to thank Martijn Schouten, Dimitrios Kosmas and Remco Sanders for their help in the laboratory. I will never forget this very meaningful happy time.

Third, thanks to my family and my girlfriend, Yujia Liu. They gave me great encouragement and support during this time.

Finally, thank all the teachers, classmates, relatives and friends who helped me in this thesis process. Without your help, I cannot finish this job smoothly.

Jiahao Cui
Enschede, December 2020

Contents

1 Introduction

1.1 Context

This project is part of the PortWings project, which revolves around research on bird flight with a robotic bird and the research is done within the NIFTy group. The main content of the project is to explore the characteristics of the 3D printed flow sensor and the feasibility to work in a control system. Therefore, the project is mainly divided into two parts. The first part is investigating, designing and fabricating a flow sensor by 3D printing technology. The second part is mainly to study the working characteristics of this kind of sensors in the control system.

In the NIFTy group, some research on tactile sensors has achieved some results, like in [1] and [2]. In the above research, a tactile sensor has been printed and some analysis has been made. This project will extend this research to investigate the possibility that can be used as a flow sensor and further improve accuracy and stability. For the second part, the project will use the sensor in a control system to explore its practicality and working characteristics. In the experiment a real closed-loop control system will be built, and the 3D printed flow sensor will form the feedback loop of this control system. Therefore, the control system will improve its controlability through the feedback signal of the sensor.

1.2 Problem Statement

In recent years, 3D printing technology has played an increasingly important role in production and life. And in the production of flow sensor, this technology also has great potential to explore. Compared with other traditional manufacturing technologies, it has many outstanding advantages. The most important of these advantages is that the 3D printed flow sensor is made of flexible materials. Therefore, it is possible to use them in some soft structures, such as soft robots or the joints of some robots [3].However, using such 3D printing technology to manufacture flow sensors for a control system also brings many challenges.

First of all, due to the limitations of 3D printer printing methods, the shape and size of sensors should be carefully considered. At the same time, the characteristics of the measured air flow and the sensor must be matched with each other. Secondly, the method of generating the airflow is to use propellers. This airflow is not very stable and can not be well detected, which will also bring certain challenges to the research. In addition, due to the influence of 3D printing materials, the sensor will have non-linearities like hysteresis and creep due to e.g. the visco-elastic properties, therefore, the control system can also be affected by these problems.

1.3 Related Work

Before starting research, relevant theories and results need to be researched. The main research direction of this project is to explore the feasibility of 3D printing flow sensors and exploring their working characteristics, in particular in a close-loop control system. So the main concern of this work is 3D printing sensors.

1.3.1 3D printed flexible sensor based on piezo-resistive sensing

There are many types of 3D printed sensors. Among them, sensors based on the piezo-resistive principle are worthy of being studied, just like in [1].This sensor uses 3D printing technology to print conductive and non-conductive materials together which is shown in (Fig. 1.1). The change in the resistance of the conductive material when the flexible sensor is deformed is used to measure a force. In the application as flow sensor, this force is produced by the drag on the sensor due to the air flow.

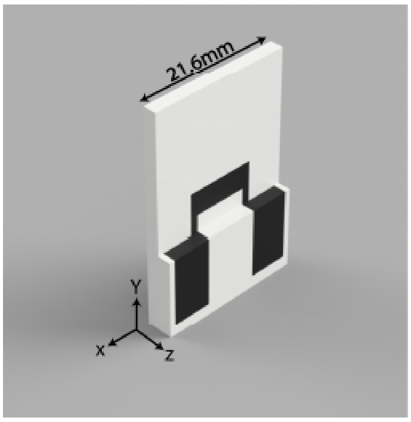

Figure 1.1: Sensor based on piezoresistive sensing [1]

1.3.2 Application of bionic theory flow Sensor

The design of flow sensors is also very diverse, some of which are bio-inspired. As in [4](see in Fig. 1.2) and [5], the shape design of these flow sensors refers to the sensory organs of some animals in nature, such as the hair-flow sensors of insects or flow-receptors of fish. This design has some advantages. From [5], these sensors generally appear in groups, and form a redundant sensing systems. In addition, redundant sensing systems may provide more information about sensor data's temporal and spatial distribution, which is difficult to obtain from point sensors.

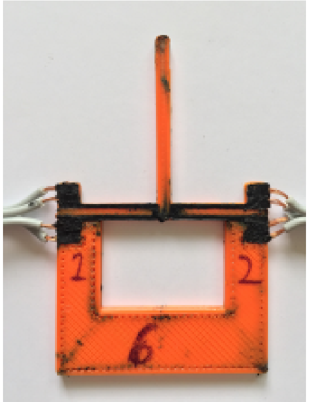

Figure 1.2: Printed whisker [4]

1.4 Objectives

The subobjectives of this project are to design and use 3D printing technology to manufacture a flow sensor, and explore the working possibility of it in a closed-loop control system. The main objective can be broken down into the following tasks:

1. Design: the first step is the modelling and design of the flow sensor. This design should meet a certain degree of sensitivity to flow velocity, and allow fabrication by 3D printing.
2. 3D printing: the second task is the 3D printing of the flow sensor. This part needs to result in a physical realisation of the previous designed model.
3. Characterisation: the third task is to identify the static and dynamic characteristics of the sensor.

4. Control system: the task of the fourth part is to design and build the control system. Then conduct experiments to explore the working characteristics of this flow sensor in the control loop, and analyze the experimental data.

1.5 Report Structure

The report is mainly divided into two parts. The first part is the design and printing of the flow sensor. The second part is mainly to design some experiments to analyze the characteristics of this sensor and explore its practical application capabilities.

Chapter 2 of the report mainly discusses the design part of this project which includes concept design, sensor design and control system design. Chapter 3 describes the printing work of the sensors. Chapter 4 mainly introduces all the experimental setups and methods used in this project. The results of the experiments of Chapter 4 are shown in Chapter 5. Finally, Chapter 6 presents some discussions and conclusions of this project.

2 Design

2.1 Introduction

This chapter introduces the design part of this project. It includes the conceptual design of the sensor, the design of the sensor and the preliminary design of the control system. The most suited solution among several concepts is selected and the corresponding sensor model and control system are designed based on it. In the sensor design part, the mechanical and dynamic model of the sensor will also be discussed in detail.

2.2 Concept design

2.2.1 Materials

3D printed materials are very important for the entire project. This project uses the PI-ETPU 85-700+ [6] with carbon black particles infused. This material has approximately the same flexibility as other thermoplastic polyurethane (TPU), and it is also a conductive material with piezoresistive properties. Therefore, when this TPU is deformed, its resistance will change according to the deformation. In this material there is a network of carbon particles. When this TPU is stretched by an external force, the carbon network will also change. This change in the layout of the carbon network is related to the extra length obtained by the material and can be measured. In addition to this conductive material, there is also a non-conductive TPU materials: Ninjaflex [7]. As the PI-ETPU, This material is relatively flexible, slightly even more so, and can be applied to the design of sensors.

2.2.2 Measurement method

There are some ways of measuring flow by a sensor with conductive TPU. A good method of measuring a flow or pressure is to integrate loops of conducting material in the structure where the change in resistance is measured upon deformation. Obviously, the best position to place these conductive materials on the sensor is where the deformation is greatest. When the sensor is stretched, both the resistivity of the conductive material as well as its geometry will change, and its resistance will also change. This method is simple and can be accurate.

If only one loop is used in the measurement, some problems will occur. Under this measurement, the resistance will be $R+\Delta R$. R is the resistance of the sensor when there is no air flow, and ΔR represents the change in resistance, which is also discussed in [1]. Therefore, if you want to calculate ΔR, R needs to be known first. This would be fine if the materials in the sensor always return to their original shape. However, the material properties of TPU determine that it will neither simply change to a certain deformation when stressed, as there is a certain amount of creep, nor return to its original shape after each deformation, because it has a certain drift. If measured in this way, huge errors that cannot be ignored will occur. To deal with this problem, a second loop needs to be added to the measurement. Therefore, the two circuits can be used for differential measurement. In this way, the error caused by such a drift will disappear, because only the difference of the resistance is calculated, and the original value of the resistance will no longer be important. Of course, this must be based on the premise that the drift generated by the two circuits is equal.

2.2.3 Concept models

First, the shape concept of the sensor need to be determined. The overall concept is that flow impacting on a deformable, cantilever like structure, excerts hydrodynamic forces on this structure by (viscous, laminar or turbulent) drag, thereby deforming the structure. Several different geometries will be discussed.

The first concept is a flat model which is shown in figure. This model is in essence a flat plate perpendicular to the flow of air.

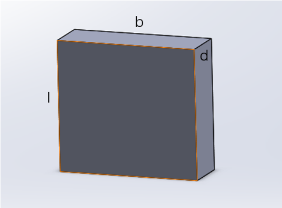

Figure 2.1: Concept 1: flat model

The second concept is another form of concept 1. It has a larger height and a shorter width, seen in (Fig. 2.2). Its overall shape is more like a cuboid.

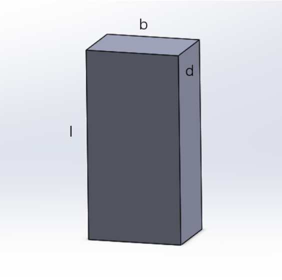

Figure 2.2: Concept 2: cuboid model

The third concept is an improved version of concept 1. In order to increase the bending degree of the sensor, a small flat is added under the original flat. Its appearance is shown in (Fig. 2.3). Compared to concept 1, it definitely has better sensitivity.

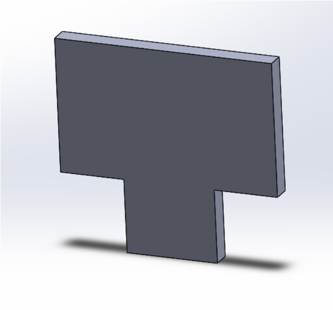

Figure 2.3: Concept 3: improved flat model

The fourth concept is a hair model, seen in (Fig. 2.4). Its shape resembles a hair, and it is an elongated cylinder. This concept will cause a smaller resistance to the aircraft than square plates. However, this shape is not easy to make using 3D printing technology. And because of its small size, it is difficult to add a strain gauge to the sensor. Therefore, the pizeo-resistive strain gauge planned to be used in this project is not suitable for this concept.

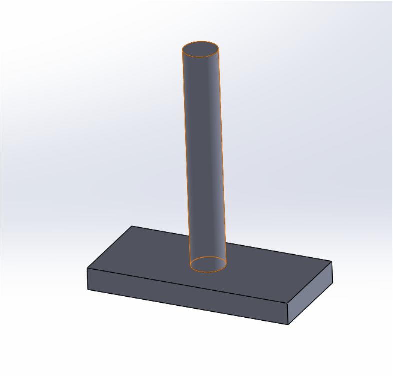

Figure 2.4: Concept 4: hair model

2.2.4 Conclusion of concept design

In summary, the advantages and limitation of each concept are introduced in the table 2.1.

Concept	Advantages	Limitation
1	Easy to print, requires low accuracy	Creates much drag
2	Easy to print, creates little drag	Low sensitivity
3	High sensitivity	Creates much drag
4	Creates little drag	Hard to print

Table 2.1: The advantages and limitation of various concepts

When comparing these concepts, concept 4 is the most difficult to print, and the material properties of TPU make it difficult to support this slender structure. So it may be possible to try this concept by using other materials and technologies. Concept 1 and concept 2 are easier to print, but the degree of bending is not as great as concept 3. In the experiment, if the bending degree of the sensor under flow is too small, it will directly affect the measurement of the data and reduce the sensitivity of the sensor. Concept 3 is feasible in printing technology, and under the same speed of airflow, it has a greater deflection than concept 1 and 2.

Through the above comparison and analysis, concept 3 is the best choice. Compared with other designs, it has the highest feasibility.

2.3 Sensor design

This part of the report will introduce the design of the sensor, which mainly includes the analysis of the sensor's mechanical model, dynamic model and the selection of shape parameters.

2.3.1 Mechanical model

The model that is used is the improved flat plate concept 3. It consists of three parts: the bottom connection part, the middle bending part, and the top stiff part. The middle bending part is regarded as a cantilever beam. Only the force on the top stiff part due to the air flow is considered, but this part is regarded as a rigid body and does not show bending. The middle part will bend due to the torque on the top part, but the force of middle part is ignored because its area is very small. In Fig. 2.5, ω (N/m) is the uniformly distributed load per unit length on the sensor, l is the length of the bending part, l' is the length of the rigid part and $\delta_{\max}$ is the displacement in the x direction at the end of the bending part.

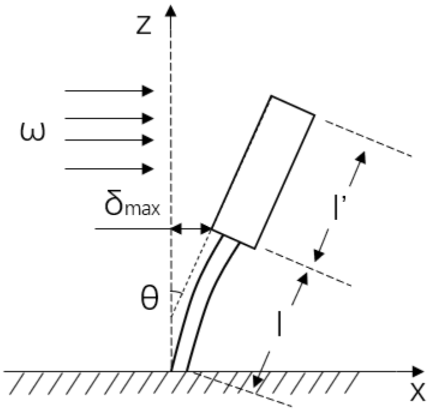

Figure 2.5: Side view of the top stiff part and middle bending part of the sensor when compressed

Beam equations

According to the geometric relationship in the graph, the middle bending part is regarded as a cantilever beam. Because θ is a very small angle, it can be approximated that $\sin(\theta) \approx \theta$. Then the following relationship can be obtained from beam theory [8]:

$$\theta(z=l) = \frac{Fl^2}{2EI} = \frac{3\delta_{\text{max}}}{2l} \tag{2.1}$$

Where F(N) represents the force on the top stiff part of sensor. Therefore, the maximum deflection(δ_{max}) at middle part's end can be known:

$$\delta_{\text{max}} = \frac{Fl^3}{3EI} \tag{2.2}$$

In this design, the main body of the sensor is mainly composed of non-conductive Ninjaflex filament. Ninjaflex has a modulus of E=12 MPa [9]. But because the sensor includes ETPU, its overall Young's modulus should be slightly greater than 12 MPa. ETPU has a higher modulus than Ninjaflex, because the carbon particles in it have inflexible characteristics. I represents the second moment of inertia of the beam, and b' is the width of middle bending part.

$$I = \frac{b'd^3}{12} \tag{2.3}$$

The force can be written by the distributed load of a function of the flow velocity:

$$F = \omega l' = \frac{1}{2}C_{\text{D}}Dv^2bl' \tag{2.4}$$

The influence of the boundary layer is ignored here, and some approximations are made. In this equation, C_{D} is the drag coefficient of the the sensor shape, D (kg/m^3) is the density of the flow, v (m/s) is the flow velocity. The drag coefficient of a flat plate positioned perpendicular to the flow is equal to $C_{\text{D}} = 1.28$ [10]. The density of air at a temperature of 15 degrees can be taken as $D = 1.225\,\text{kg/m}^3$ [11]. And b represents the width of stiff top part.

So then the equation can be written as:

$$\delta_{\text{max}} = v^2\frac{C_{\text{D}}Dbl'l^3}{6EI} \tag{2.5}$$

Strain

In order to calculate the deformation of the sensor by measuring the change in resistance, the fiber strain of the strain gauges needs to be confirmed. Fig. 2.6 shows the induced strain when the sensor is bent. The two left and right shaded part at the bottom of the sensor represent strain gauges.

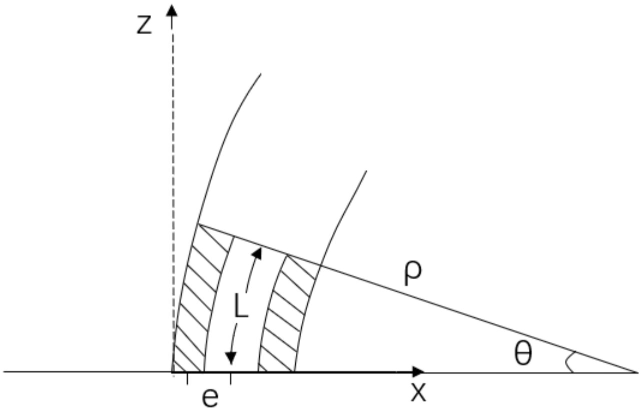

Figure 2.6: Sensor strain in deformation

From the (Fig. 2.6), it can be seen that:

$$L = \rho\theta \tag{2.6}$$

Where ρ is the approximate radius of the circle created by the bending of the sensor. This approximation can only be performed on a small displacement at the bottom of the sensor. In (Fig. 2.6), e represents the distance from the neutral axis of the beam to the center of the strain gauge. ΔL is the difference in length between the center of the beam and the center of the left strain gauge. This also implies that:

$$\frac{L}{\rho} = \frac{\Delta L}{e}, \frac{\Delta L}{L} = \frac{e\theta}{L} \tag{2.7}$$

According to formula (2.1) and formula (2.7), the following equation can be obtained. The following equation can now be used to transform a given deflection to the end of the model to the strain in the strain gauges.

$$\frac{\Delta L}{L} = \delta_{\text{max}} \frac{e}{lL} \tag{2.8}$$

Finally, two equations (2.5) and (2.8) are combined, and the final result between the flow velocity with the strain can be drawn:

$$v = \sqrt{\frac{\Delta L}{L} \frac{6EIL}{C_{\text{D}} Dbel^2 l'}} \tag{2.9}$$

2.3.2 Calculation and results

According to the above analysis, in order to calculate the deformation of a particular model to a certain extent under air flow, one must first determine the external dimensions. With reference to the existing experimental results, first select an external dimension for calculation and then adjust if the result is unreasonable. The following Fig. 2.7 shows the shape of model 3. The gray parts in the picture are non-conductive materials, and the black parts are strain gauges which should be printed by ETPU. Based on the work in [1], first try the top stiff flat: l×b×d=14×20×1.6(mm^3). The middle bending flat : l×b×d=6×10×1.2(mm^3). The bottom connection flat: l×b×d=10×20×1.6(mm^3). Also, first set the thickness of the sensor to 1.2 (mm).

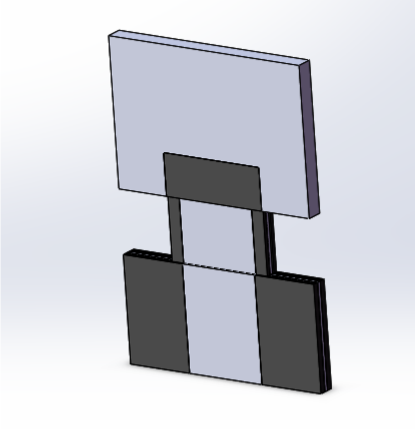

Figure 2.7: Sensor design in Solidworks

The shape of the strain gauge on the sensor is shown in (Fig. 2.8) based on the results in [1]. The dimensions in this figure are in (mm). According to the previous design, the thickness of the strain gauge should be one-third of the overall thickness, so its thickness is 0.4 mm.

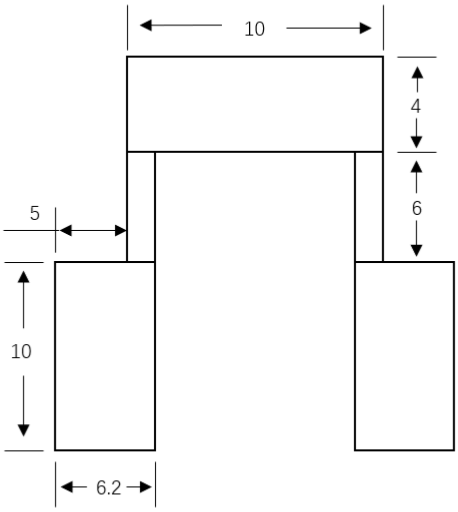

Figure 2.8: Strain gauge geometry, dimensions in mm.

The results can be calculated using the previous formula for concept 3, and first, the flow velocity will be assumed to be $15\,\mathrm{m\,s^{-1}}$. $\delta_{\max}$=1.715 mm. $\frac{\Delta L}{L} = 0.0043$. This maximum deflection value is appropriate to the overall size of the sensor, but in Chapter 3, the actual size of the sensor will be adjusted according to the printing situation.

According to the previous analysis, there are two strain gauges on each side of the sensor, so the total ΔR/R can be obtained by the following equation:

$$\frac{\Delta R}{R} = \frac{1}{4}\left(\frac{\Delta R_{\text{Front}}}{R_{\text{Front}}} + \frac{\Delta R_{\text{Back}}}{R_{\text{Back}}}\right) \tag{2.10}$$

2.3.3 Conclusion of sensor design

In this part, a feasible flow sensor is designed, which uses concept 3 (improved flat model) discussed in concept design section. In addition, this part focuses on the mathematical model of this flow sensor and the relationship between flow velocity and sensor deformation is obtained through calculation. The correctness of this relationship will be verified through experiments later in chapter 5.

2.4 Dynamic model

The previous part of this chapter gives the relation between flow velocity and strain, but the information on the dynamic behaviour of the sensor also needs to be known.

First, an approximate analogy to the sensor model is made. The middle bending part of the sensor is thought of as a rotation spring and the top stiff part as a rigid body with mass M and Moment of inertia J around the rotation axis. This is because in the experiment, the stiff part hardly bends, and the midpoint of the thin part is regarded as the center of rotation, which is consistent with the first case in the pseudo-rigid-body(PRB) model [12]. The resulting model is (Fig. 2.9).

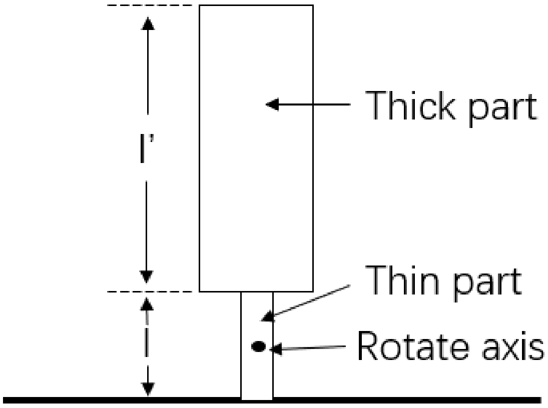

Figure 2.9: Sensor rotate model

The entire system is modelled as a lumped second order system and the following formula describes the movement of the entire system [13].

$$J\frac{d^2\theta}{dt^2} + C\frac{d\theta}{dt} + k\theta = \tau(t) \tag{2.11}$$

In this equation, J represents the Moment of inertia, C represents angular damping constant, k represents torsion spring constant, τ represents drive torque.

If the damping is small, $C \ll \sqrt{\frac{\kappa}{J}}$, as is the case with torsion pendulums and balance wheels, the frequency of vibration is very near the natural resonant frequency of the system:

$$f_\mathrm{n} = \frac{\omega_\mathrm{n}}{2\pi} = \frac{1}{2\pi}\sqrt{\frac{\kappa}{J}} \tag{2.12}$$

Therefore, the period is represented by

$$T_\mathrm{n} = \frac{1}{f_\mathrm{n}} = \frac{2\pi}{\omega_\mathrm{n}} = 2\pi\sqrt{\frac{J}{\kappa}} \tag{2.13}$$

According to the pseudo-rigid-body model, $k = \frac{(EI)_l}{l}$, where $()_l$ represents the parameters of the middle bending part. Moment of inertia of the top stiff part can be describe as the following equation:

$$\begin{aligned}
J &= \int_{-t/2}^{t/2}\int_{l}^{l+l'}\int_{-w/2}^{w/2} \rho x^2 dt dx dw && (2.14)\\
&= \rho t w \frac{1}{3} x^3 \Big|_{l}^{l+l'} && (2.15)\\
&= \frac{\rho t w}{3}\left\{(l+l')^3 - l^3\right\} && (2.16)\\
&= \frac{\rho t w}{3}\left\{l^3 + l'^3 + 3ll'^2 + 3l^2 l - l^3\right\} && (2.17)\\
&= \frac{\rho t w l}{3}\left\{l'^2 + 3ll' + 3l^2\right\} && (2.18)\\
&= M\frac{1}{3}\left\{l'^2 + \frac{3}{2}ll' + \frac{3}{4}l^2\right\} && (2.19)
\end{aligned}$$

And because the rotation point is in $l/2$, the relationship will become:

$$J = M\frac{1}{3}\left\{l'^2 + \frac{3}{4}ll' + \frac{3}{16}l^2\right\} \tag{2.20}$$

Where M represents the mass of the stiff part. Finally, the natural frequency can be obtained as:

$$f_\mathrm{n} = \frac{1}{2\pi}\sqrt{\frac{(EI)_l}{Jl}} \tag{2.21}$$

2.5 Control system design

2.5.1 PI controller system

The main working principle of the control system is shown in (Fig. 2.10). This experiment mainly explores the working characteristics of this 3D printing flow sensor in a control system. As shown in the figure, the control loop is built in MATLAB simulink. It includes reference, feedforward loop and PI controller. Feedforward loop is mainly to ensure the stability of the control signal, but in order to verify the ability of the sensor, white noise is introduced to interfere with the control signal. In order to increase the work proportion of the feedback loop, noise is needed to affect the signal of the feedforward loop. In this way, the signal of the feedforward will be slightly different from the reference, and the role of the controller will be more obvious. The control signal is sent to the motor through MATLAB to change the flow velocity, and the sensor detects this change to form the feedback loop of this system. This experiment will use the Arduino uno to measure the resistance change value of the sensor to calculate the current flow velocity and send the data back to the PI controller in Simulink.

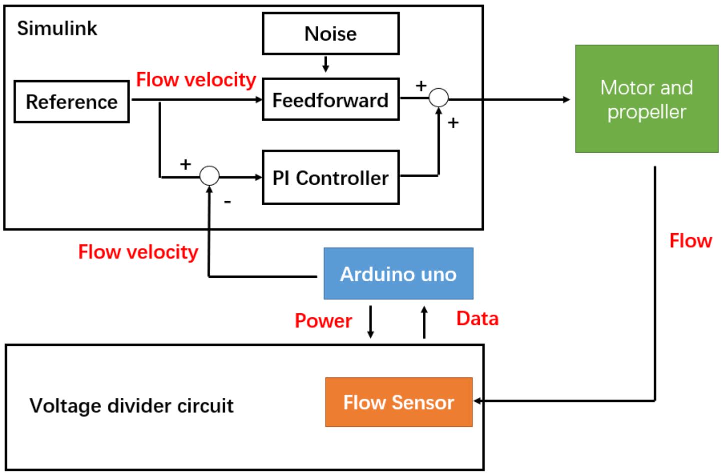

Figure 2.10: Control system block diagram

Based on this design, the basic workflow of this control system is to first input a set value, a constant value or trajectory. Next, verify that the control system can use the feedback loop including the sensor to complete the control.

2.5.2 Velocity feedback control

In order to further improve the control ability of the control system to the second-order system, velocity feedback control [14] was introduced. This control method can effectively increase the damping of the second-order system to make it faster and stable. The schematic diagram of the method is shown in (Fig. 2.11).

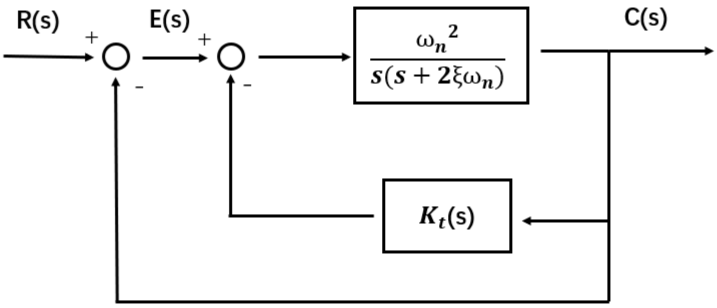

Figure 2.11: Velocity feedback control method block diagram

In this figure, ζ is damping factor, and the natural frequency $\omega_n = 2\pi f_n (\mathrm{rad\,s^{-1}})$. The closed-loop transfer function of a normal second-order system is:

$$G(s) = \frac{\omega_n{}^2}{s^2 + 2\zeta\omega_n s + \omega_n{}^2} \tag{2.22}$$

Where:

$$\zeta = \frac{1}{2Q} \tag{2.23}$$

In equation(2.23), Q represents the quality factor of the second order system. After using speed measurement feedback control, which is the $K_{\mathrm{t}}(S)$ block in the figure, its closed-loop transfer function becomes:

$$G(s) = \frac{{\omega_{\mathrm{n}}}^2}{s^2 + 2\zeta_{\mathrm{t}}\omega_{\mathrm{n}}s + {\omega_{\mathrm{n}}}^2} \tag{2.24}$$

where:

$$\zeta_{\mathrm{t}} = \zeta + \frac{1}{2}K_{\mathrm{t}}\omega_{\mathrm{n}} \tag{2.25}$$

Therefore, the damping factor of the new system will be larger than the original, which depends on the value of k_{t}. This change will reduce the oscillation time of the system, so that it can stabilize more quickly.

2.6 Conclusion

At the end of this chapter, most of the design work of this project is introduced. A suitable sensor design concept is determined, and a sensor model is designed accordingly. The mechanical model and dynamic model of this design is analyzed, and a rough control system is designed. The next chapter will introduce the manufacturing process of the sensors.

3 Fabrication

3.1 Introduction

During the production of this project, multiple sensors were 3D-printed. The detailed information of the printing device and each sensor will be discussed. Each model is changed from model 1 designed in chapter 2, with slightly different parameters.

3.2 Equipment, Material and Software

The main equipment used in this manufacturing process is the Diabase H-series Multi-Material 3D printer [15] see (Fig. 3.1). This multi-material 3D printer can print up to five different materials in one project.

For the material, PI-ETPU is used for the conductive parts, Ninjatek TPU for the non-conductive parts and E-Sun PVA [16] soluble support filament for support of the printed part.

For the software, in this project Solidworks is used to make a model for each sensor. Simplify3D is used as slicer.

Figure 3.1: Diabase H-series Multi-Material 3D printer.

3.3 Samples

A total of 14 samples were printed, of which model 1 is the same as concept 3 mentioned earlier, and models 2, 3, 4, 5 and 6 are obtained by simple modification based on model 1. All 14 sensors have relatively good print quality.

3.3.1 Model 1

Model 1 same as the concept 3 is printed first, and the print result is shown in (Fig. 3.2). After the actual printing, two problems were found. First of all, the overall sensor is too stiff if the printing directly according to the previously designed parameters. Second, because there is no non-conductive material on the edge of the sensor, therefore, strain gauges on both sides of the sensor is easily to contact each other. So, some modifications to model 1 are made to achieve better print results.

Figure 3.2: The first sensor printed with model 1

The side view of the sensor is shown in (Fig. 3.3), where the white area represents the non-conductive Ninjaflex material and the black area represents the conductive PI-ETPU material. In the middle part of the sensor both sides have the same two strain gauges. The bottom part is mainly support and connection part. In the experiment, the bottom part is mainly responsible for connecting with the measuring equipment. The black material in the top part also connects the strain gauges on the left and right sides without bending.

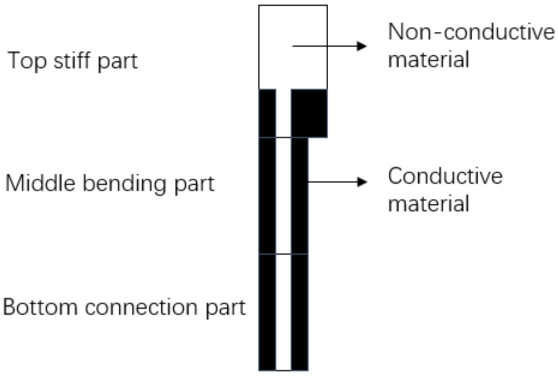

Figure 3.3: Sensor side view

3.3.2 Model 2

Model 2 has made some modifications based on model 1. First of all, they are expanded at the edge area, so that the strain gauges have a certain distance from the edge of the sensor, and the strain gauges on both sides will not connect to each other. Secondly, these three different sensors also have different thickness. The shape of this new model is shown in (Fig. 3.4).

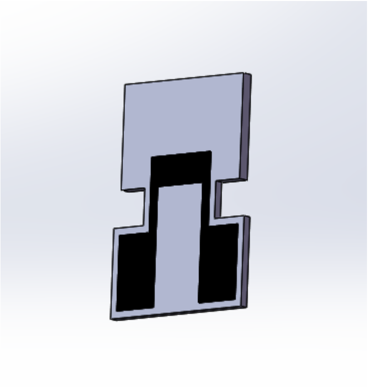

Figure 3.4: Model 2

The size parameters of sensor 3 and sensor 4 are basically the same as those of model 1. The thickness of the connection area at the bottom of the sensor is 1.2 mm, of which the thickness of the two strain gauges is 0.4 mm and the middle layer is 0.4 mm. They are shown in (Fig. 3.5).

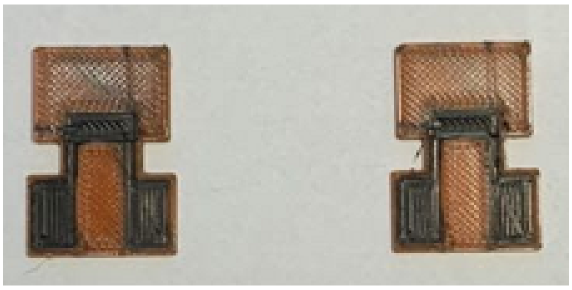

Figure 3.5: Sensor 3 and 4

Sensor 1 and 2 are thinner than sensor 3 and 4. The thickness of the bottom is 0.9 mm, two of the strain gauges are 0.3 mm thick, and the middle layer is 0.3 mm thick. Therefore it is more sensitive than the first two.

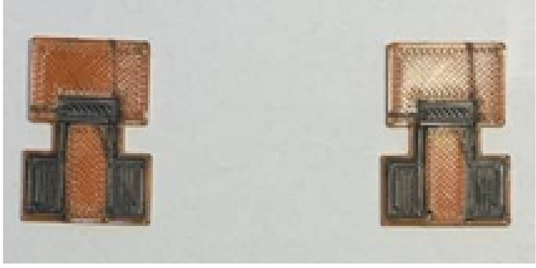

Figure 3.6: Sensor 1 and 2

Sensor 0 is the thinnest sensor. The bottom is only 0.6 mm thick. Each of the strain gauges is 0.2 mm thick and the middle layer is 0.2 mm thick. Its appearance is shown in (Fig. 3.7).

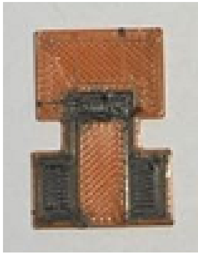

Figure 3.7: Sensor 0

3.3.3 Model 3

Model 3 is an enlarged version of the previous sensors. In order to have a more obvious deformation of the sensors under the same flow velocity, the size of the sensors is increased. In this way, the area of the force receiving part of the sensor becomes larger, so as to obtain a larger amount of deformation. In addition, in order to prevent deformation of the top stiff part of the sensor, three protruding vertical lines are added to increase the rigidity of this part. The shape of the sensor and the shape of the strain gauge are shown in (Fig. 3.8).

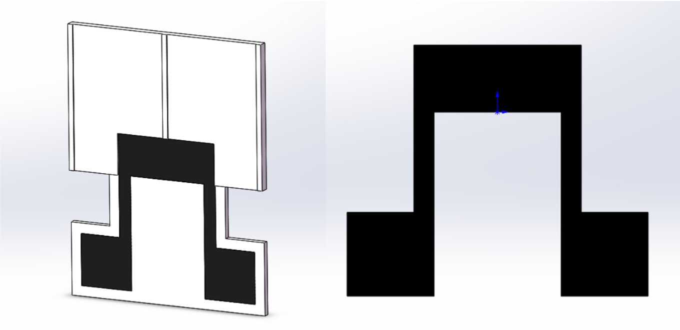

Figure 3.8: Model 3 with strain gauge

First, the thinnest sensor 5 was printed, its thickness is 0.6 mm. Second, the sensor 6 and sensor 7 which have thickness of 1.2 mm were printed. And they are all shown in (Fig. 3.9). In order to increase the conduction efficiency of the connecting part under the sensor, silver paint was applied to sensors 5 and 6, which can also be seen from the figure.

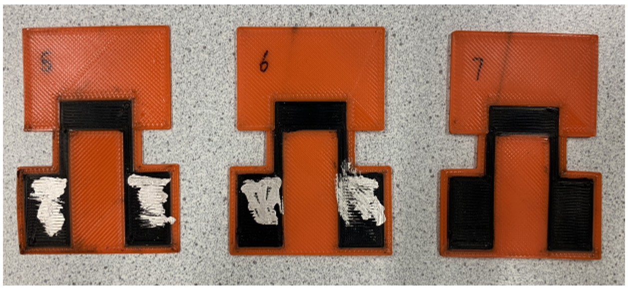

Figure 3.9: Sensor 5, 6 and 7

3.3.4 Model 4

Model 4 is an upgraded version of Model 3. And in order to solve the problem of the different roughness of the upper surface and the lower surface when the sensor is printed, model 4 uses a support part. The sensor shape and strain gauge shape are shown in (Fig. 3.10). The red part in the figure is the newly added support part. This is a material called PVA, which can be dissolved in water. This material is printed first on the glass plate, and then the overall sensor is printed. By doing so, the roughness of the strain gauges on both sides of the sensor can be kept as consistent as possible.

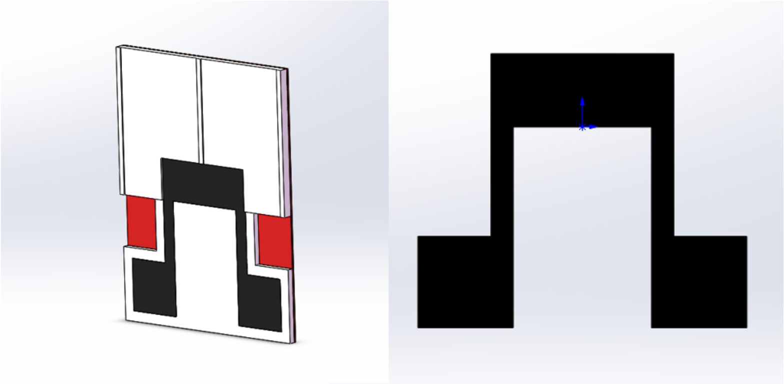

Figure 3.10: Model 4 with strain gauge

Fig. 3.11 shows the sensor 8 and 9. The sensors shown in the figure have been stripped of the support part. Their thickness is 0.9 mm.

Figure 3.11: Sensor 8 and 9

3.3.5 Model 5

According to the previous printing experience in [17], in order to further improve the characteristics of the small sensor, model 5 was designed. Model 5 is an upgraded version of Model 2, which has smaller connections which causes a lower resistance. And its strain gauge is longer. The shape of the sensor and the shape of the strain gauge are shown in (Fig. 3.12).

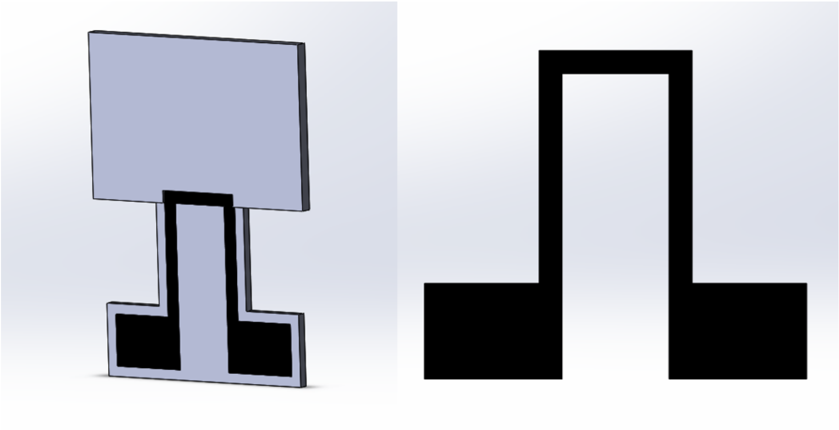

Figure 3.12: Model 5 with strain gauge

Sensors 11 and 12 with a thickness of 0.9 mm were printed, and their connecting parts were also coated with silver paint to improve conductivity.

Figure 3.13: Sensor 10 and 11

3.3.6 Model 6

Model 6 is an upgraded version of Model 5. The two strain gauges on each side of it are closer together. This design can make the deformation of the strain gauge larger and minimize the influence of its connecting bridge part. The sensor shape and strain gauge shape are shown in (Fig. 3.14).

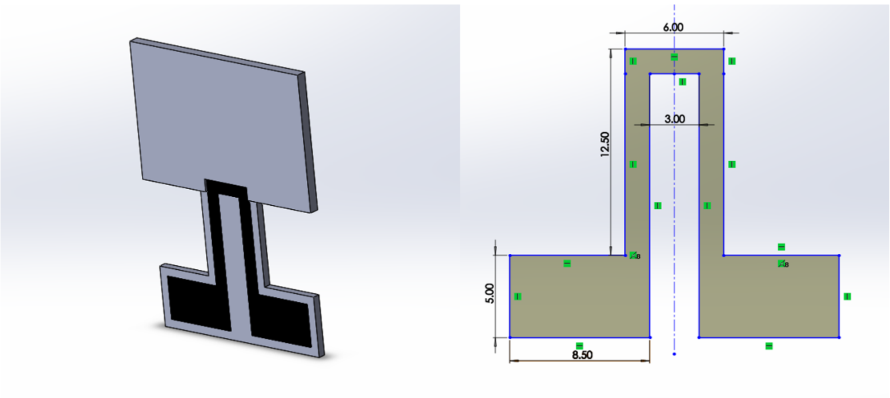

Figure 3.14: Model 6 with strain gauge

Sensor 12 and sensor 13 with a thickness of 0.9 mm are printed according to model 6. The specific parameters of its strain gauges are shown in the figure too, and the unit is (mm). Finally, the overall size of model 6 is: The top stiff flat: l×b×d=16×24×1.2(mm^3). The middle bending flat : l×b×d=10×10×0.9(mm^3). The bottom connection flat: l×b×d=7×22×0.9(mm^3).

Figure 3.15: Sensor 12 and 13

3.4 Conclusion

The Fig. 3.16 shows all the sensors from 0 to 13 printed in this project.

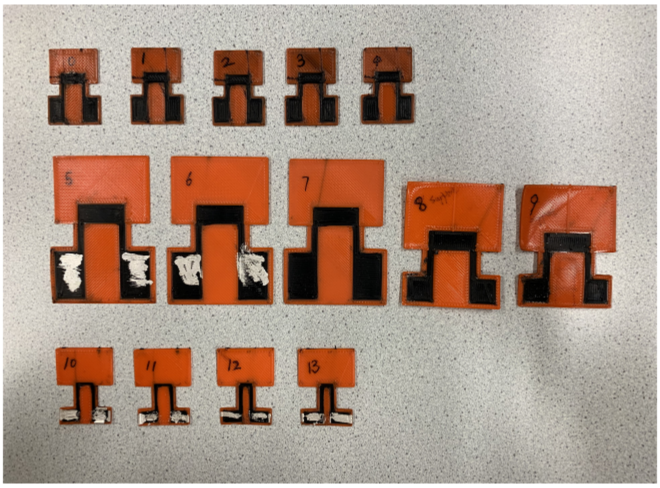

Figure 3.16: All Sensors

And, the basic information of all sensors is shown in the table below.

Number	Type	Thickness(mm)	Remarks
0	model 2	0.6	Thickness is too thin, the resistances on both sides are connected.
1	model 2	0.9	Good print quality
2	model 2	0.9	Good print quality
3	model 2	1.2	The thickness is too large to produce effective deformation.
4	model 2	1.2	The thickness is too large to produce effective deformation.
5	model 3	0.6	Too thin
6	model 3	1.2	Good print quality
7	model 3	1.2	Good print quality
8	model 4	1.2	Resistance change is not obvious
9	model 4	1.2	Resistance change is not obvious
10	model 5	0.9	Good print quality
11	model 5	0.9	Good print quality
12	model 6	0.9	Good print quality
13	model 6	0.9	Good print quality

Table 3.1: Information of Sensors

According to the analysis, model 6, namely sensor 12 and sensor 13, will be the best sensors. Because they have the longest strain gauges among small sensors, it also means that they will have the greatest resistance change under same flow velocity. In addition, compared to other sensors, they has the smallest bottom connection part and connection bridge (the connection part of two strain gauges on the same surface), so it should have the smallest total resistance. According to the above two reasons, sensors 12 and 13 should be the most sensitive of all small sensors. In chapter 5, some experiments will be used to verify these inferences.

4 Experimental Methods

4.1 Introduction

This chapter will introduce several experimental principles and set-ups used for analyzing the sensors printed in chapter 4 and explore their performance in practical applications. These experiments include initial experiments with a small propeller, mechanical sensor characterization, dynamic analysis experiment and control system experiments.

4.2 Initial experiment

In order to better understand these printed flow sensors, this project will give a preliminary understanding of the characteristics of each sensor through experiments. This experiment mainly explores the range and stability of sensor resistance changes under airflow of a small propeller.

4.2.1 Experiment setup

The principle block diagram of this experiment is shown in (Fig. 4.1). As shown in the figure, the experiment will use a small propeller driven by a DC motor to generate an airflow. The two strain gauges of the sensor are connected to two half voltage divider circuits, and their signals will be used as input of the Arduino uno [18], a microcontroller board, to measure their resistance changes. In order to improve the measurement resolution of the Arduino, a 16bit ADC module called DFRobot ADS 1115 [19] is used.

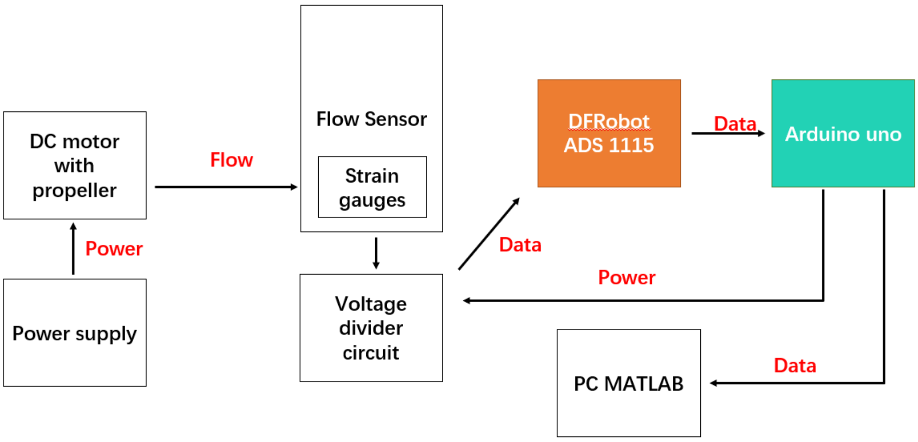

Figure 4.1: Initial experiment method block diagram

Next, each experimental device will be discussed in detail.

Voltage divider circuit

The circuit includes two independent voltage dividers, as shown in (Fig. 4.2). The two fixed value resistors are chosen to be similar to the resistance of the sensor strain gauges. In the picture, $V1$ and $V2$ are connected with the DFRobot ADS1115 to measure the voltages. The voltage supply is provided by the Arduino uno, and the value is 5 V.

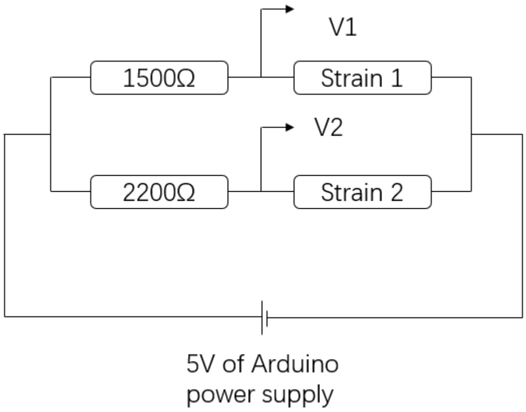

Figure 4.2: Voltage divider circuit

DFRobot ADS 1115

DFRobot ADS 1115 is a high precision ADC, it is 16bit versus 8bit for the Arduino . So it has better resolution and can give a higher precision during Arduino measurements. More detail can be found in [19].

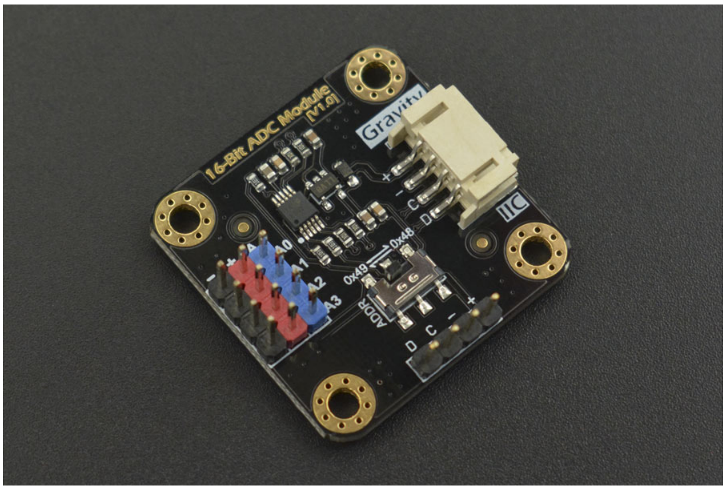

Figure 4.3: DFRobot ADS 1115

DFRobot ADS 1115‘s C and D interfaces should be connected to the SCL and ADS port of Arduino. And, its positive port and negative port should be connected to Arduino’s 5 voltage output port, and ground port.

Microcontroller

The appearance of the Arduino is shown in (Fig. 4.4).

Figure 4.4: Arduino uno

The measurement signal will be transmitted from the DFRobot ADS 1115 to the Arduino, and then converted into a resistance signal by the program in the compiling software Arduino IED, and then sent to the MATLAB of the PC.

Finally, the actual display diagram of the experimental equipment is shown in (Fig. 4.5).

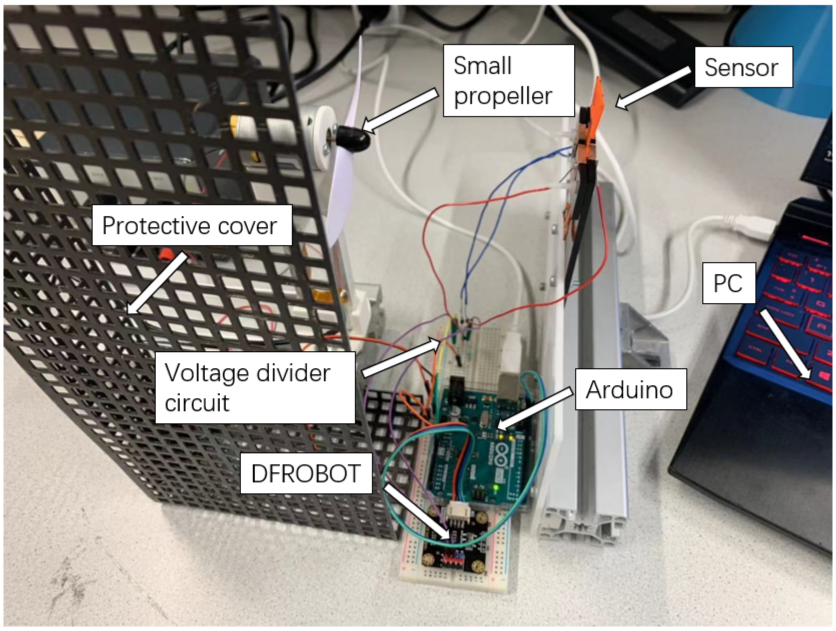

Figure 4.5: Initial experiment setup

4.2.2 Experiment plan

As can be seen from Chapter 3, all printed sensors have a rough side and a smooth side. Therefore, all sensors will conduct experiments in two directions, that is, the cases in which either the rough side faces the propeller or the smooth side faces the propeller. The experiment plan is to place 14 sensors under the same airflow and conduct experiments in two directions. Therefore, both the rough side and the smooth side's stretch and compression results will be recorded.

The experiment has two main goals. First observe the different properties of each sensor on two different surfaces in tension and compression. Secondly, compare the resistance variation range of each sensor and the stability of the signal.

4.3 Sensor mechanical characterization

This experiment mainly explores the relationship between the resistance in the strain gauge on the sensor and its deformation. This relationship is very important for the application of this sensor.

4.3.1 Experiment set-up

The main equipment and instruments required for this experiment include: a 3D printed flow sensor; an Oscilloscope (type TiePie Handyscope HS5); a SMAC linear actuator (LCA25-050-15F) with its controller; PC with MATLAB; Mechanical assembly. This set-up and measurement is based on the measurements in [1] and in [2]. The overview of the experiment setup is shown in (Fig. 4.6)

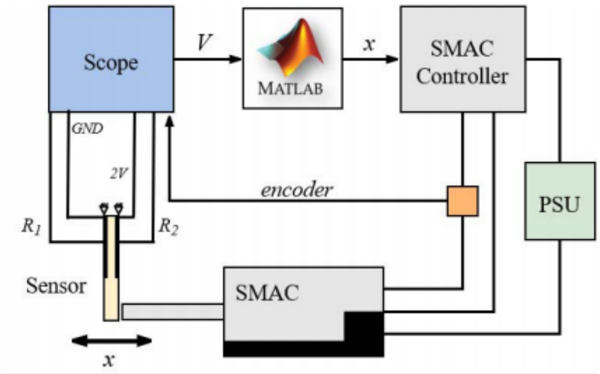

Figure 4.6: Overview of the mechanical characterization experiment set-up [2].

The main purpose of the setup is to measure voltage changes in both strain gauges of the sensor under various excitations. The following sections will introduce in detail the usage and functions of each component.

Oscilloscope

Figure 4.7: 2-Channel Handyscope HS5 module.

To measure the voltage changes of the two strain gauges on the sensor, the digital oscilloscope shown in (Fig. 4.7) is used. According to the results of [2], the oscilloscope can provide an excitation signal and measure the voltage changes of the two channels.

Linear actuator

Figure 4.8: Linear actuator: SMAC LCA25-050-15F.

The SMAC LCA25-050-15F (Fig. 4.8) is a linear actuator with a maximum stroke of 50 mm. It can be controlled with force or position.

Figure 4.9: SMAC single axis controller.

The controller (LC-10) controls this actuator. And this controller uses a feedback loop to control the system with Embedded Motion Control Library (EMCL). More details are described in [2]. Before each experiment, the initial position of the SMAC must be calibrated, and the calibration voltage is 25.2 V.

Software

The program that controls the movement of the SMAC and the program that measures the voltage of the strain gauges of the sensor are written in MATLAB. The entire system is connected in the MATLAB environment too. In addition, the measurement data processing program is also written in MATLAB. The main MATLAB code of this part can be seen in the appendix A.

Layout

A base is needed to build the entire experiment system which is a 500 mm × 500 mm × 30 mm aluminum plate. 5 mm threaded holes are evenly distributed on this aluminum plate for fixing other equipment. The 3D printed flow sensor is fixed on an aluminum bracket that can move arbitrarily in the horizontal and vertical directions. The actual display of the experimental set-up is shown in (Fig. 4.10).

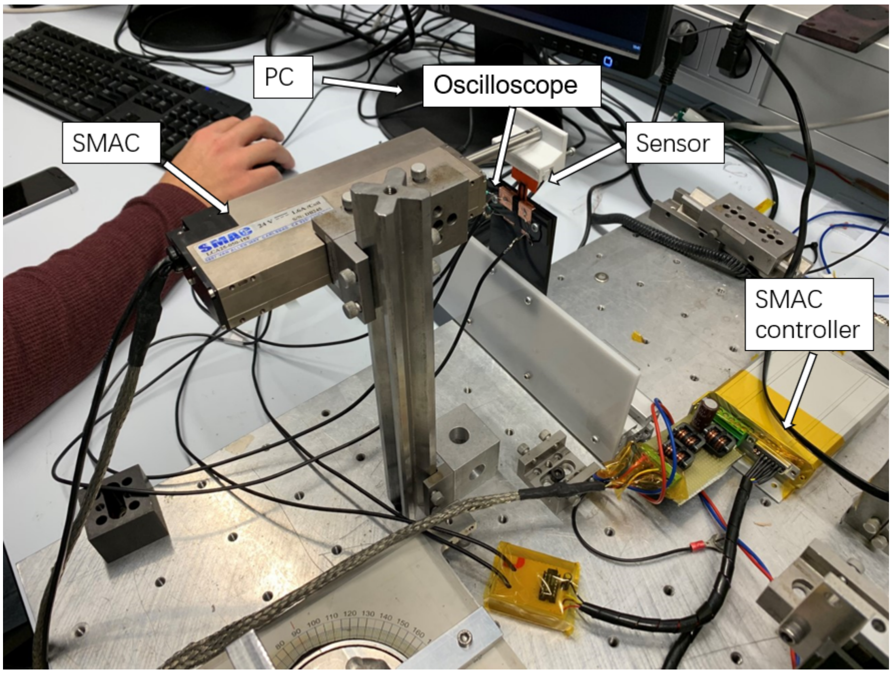

Figure 4.10: Sensor mechanical characterization setup

4.3.2 Experiment Plan

The experimental principle is to use SMAC to move the top of the sensor to make it deform, and measure the resistance change of the strain gauges on the sensors at the same time, so as to obtain the relationship between the resistance change and the sensors deformation.

First, we design an experimental circuit including two voltage dividers, as shown in (Fig. 4.2). The measurement data is the voltage value of the two strain gauges on both sides of the sensor. Then, calculate the resistance value of these two strain gauges by the power supply voltage and the resistance value of the fixed resistance. As with the previous experiment, the resistance of the strain gauge on both sides of sensor 13 can be known. Therefore, the fixed resistances of the two voltage dividers are respectively chosen as 1500 Ω and 2200 Ω, which are similar to them, so that they can have more obvious changes.

The SMAC device is used to compress and stretch the sensor head to make it produce a regular reciprocating motion. Use the digital oscilloscope to measure the voltage change of two strain gauges. The position change control of SMAC and the measurement of voltage change on the sensor strain gauges are all controlled by MATLAB program which can be seen in appendix A.

4.4 Dynamic analysis

This part will design experiments to explore the dynamic model of the sensor. First, the experimental setup will be introduced.

4.4.1 Experimental set-up

The experimental set-up is the same as in [17]. The block diagram of the experiment is shown in (Fig. 4.11).

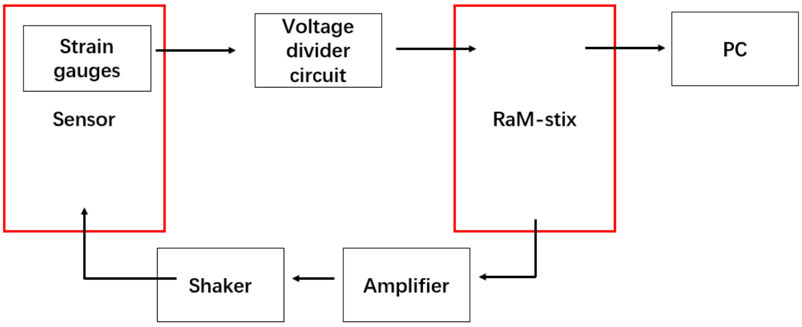

Figure 4.11: Block diagram of dynamic analysis experiment [17]

The most important equipment for the experiment is the MB Dynamics PM50A Shaker [20], which vibrates the base of the sensor. In the experiment the shaker is used to excite the sensor harmonically in a frequency sweep, going from 0 Hz to 200 Hz. The MB PM-50A shaker needs a 46 V voltage, but the RaM-stix has only 1 V analog output. So the amplifier is used to amplify the voltage by 46 times. The 20-Sim software on the RaM-stix is used to tune the amplitude, frequency, phase, start time and stop time. The actual experimental set-up is shown in (Fig. 4.12).

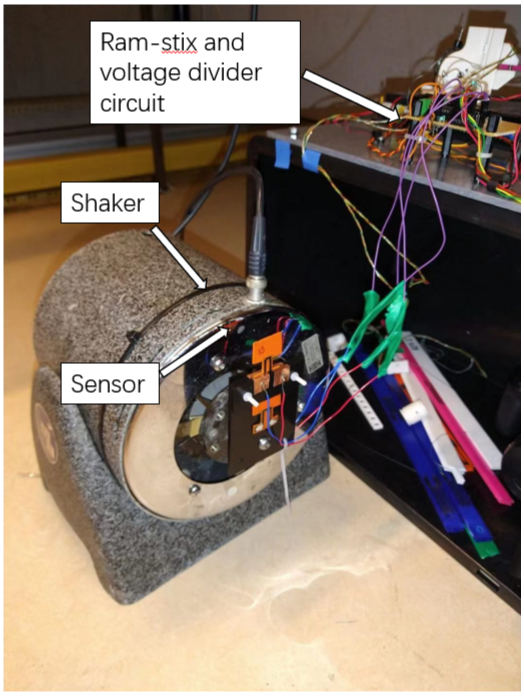

Figure 4.12: Shaker set-up

4.4.2 Experiment method and plan

The experiment uses the shaker to obtain the frequency response of the 3D-printing sensors and infer its eigenfrequency from these results. For the accuracy of the experiment, the experiment will test both sensor 12 and sensor 13. Both of them are printed with model 6, so their experimental results should be roughly the same. It has to be note that the shaker excites the base of the sensor, which yields a slightly different response from the classical excitation of the mass.

4.5 Experiment with wind tunnel

In initial experiments, airflow is generated from a small propeller. But this kind of airflow cannot be detected very accurately in the experiment. Therefore, in order to better grasp the situation of the surrounding airflow when the sensor is working, a wind tunnel will be used.

This wind tunnel is called Educational Wind Tunnel (EWT) from AEROLAB [21]. In the experiment, the sensor was placed in this kind of wind tunnel, and different flow velocities were switched to observe the performance of the sensor. The experimental plan mainly includes two different tests. First, place the sensor under constant airflow of different values and observe its performance. Second, the experiment will increase and decrease the value of the flow velocity by steps of $2\,\mathrm{m\,s^{-1}}$ to observe the residual drift in the sensor.

The real experiment set-up is shown in (Fig. 4.13). In this figure, the measurement set-up is the same as the set-up in the control system experiment.

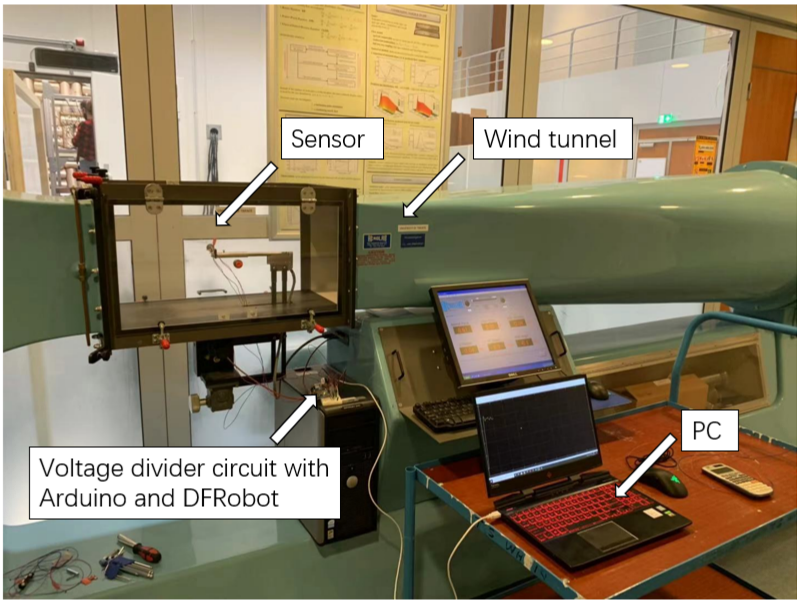

Figure 4.13: Experiment with wind tunnel set-up

4.6 Control system experiment

In this section the set-up and plan of the control system experiment is introduced. The design of the control system is roughly as described in chapter 2, and the entire experimental system will be introduced in more detail. This experiment is mainly to explore the performance of the sensors in actual control systems.

4.6.1 Experiment set-up

Simulink model

The Simulink model in the experiment is shown in (Fig. 4.14). It is mainly divided into three parts, the controller part in the red box, the sensor receiving signal part in the blue box and the control signal output part in the yellow box. The three red errors in the signal output part indicate that Simulink is not currently connected to the actual drone propeller motor.

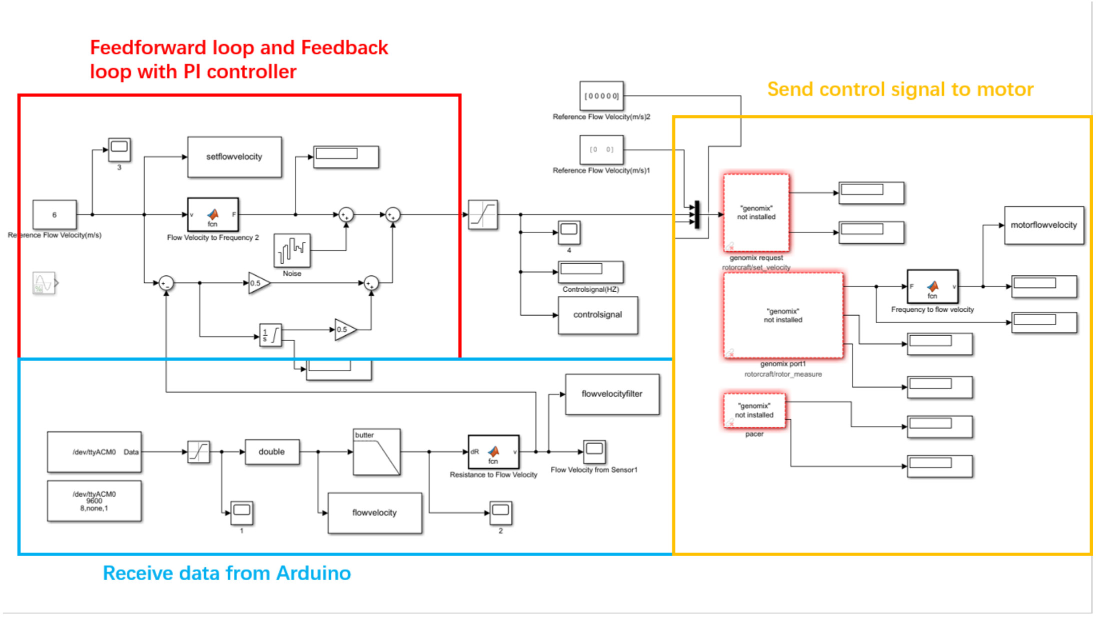

Figure 4.14: Simulink model

Flow from drone propeller

In this paper, the motor is used to drive the propeller to generate airflow. Therefore, it is necessary to determine the relationship between the airflow generated by the propeller and its rotation frequency. After a simple approximation for the flow velocities, there is an equation representing the relationship [22] between the thrust, and incoming and outgoing flow velocities:

$$T = \rho A_{\text{disk}} \frac{(v_{\text{e}} + v_{\text{o}})}{2} (v_{\text{e}} - v_{\text{o}}) = \rho A_{\text{disk}} \frac{v_{\text{e}}^2 - v_{\text{o}}^2}{2} \tag{4.1}$$

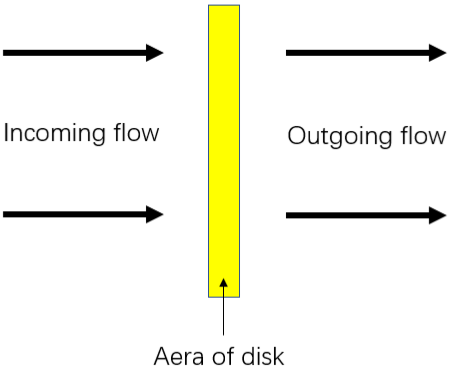

Figure 4.15: Propeller and its air flow

In this equation, T represents the thrust, v_{o} and v_{e} represent incoming velocity and outgoing velocity of the flow, A_{disk} represent the area of the disk.

According to the previous chapter, because the propeller type is fixed, the incoming velocity can be 0. A_{disk} depends on the propeller model used, so the only one parameter that needs to be determined is the thrust. From [23], a simple thrust equation is given by:

$$T = C_{\text{t}} D n^2 P^4 \tag{4.2}$$

where: T=thrust (N); C_{t}=thrust coefficient; D=density (kg m^{-3}); n=propeller revolutions per unit of time (RPM); P=propeller diameter (m); Then the following equation can be obtained:

$$A_{\text{disk}} \frac{v_{\text{e}}^2}{2} = C_{\text{t}} n^2 P^4 \tag{4.3}$$

From equation (4.3), it can be seen that, except for flow velocity and propeller revolutions, all are constants. Therefore, the flow velocity produced by the propeller is directly proportional to its rotational speed. This result can help the subsequent calibration work. The flow velocity represents the value close to the propeller, as the distance increases, this flow velocity will gradually weaken.

Control with the drone propeller

In the flight lab, the drone propeller can be controlled by the MATLAB code which is shown in appendix A. And the flow velocity can be controlled by the rotation frequency set point of the motor in the code. The actual drone propeller and motor (MK3638 Mikrokopter) are shown in (Fig. 4.16). The size of the propeller is 13×4.5R, where 13 is the diameter of the propeller and 4.5 is the pitch. Their units are all inches.

Figure 4.16: Drone Propeller

Calibration for the propeller

In order to know the actual flow velocity generated by this drone propeller at a specific rotation frequency, it should be calibrated. In the experiment, an anemometer flow sensor (Techno Line EA-3010) will be used to calibrate it. The propeller and the sensor are fixed at a mutual distance of 50 mm. The rotation frequency of the propeller is varied from 20 Hz to 90 Hz, and the actual flow velocity is recorded.

Through the previous dynamic analysis of the flow produced by the propeller, it can be expected that the flow velocity is proportional to the rotational speed of the propeller. According to this result, the curve fitting software of MATLAB can be used to perform a linear fitting through the origin. Therefore, a relation between the propeller rotation frequency and the flow velocity is obtained using MATLAB which is shown in (Fig. 4.17).

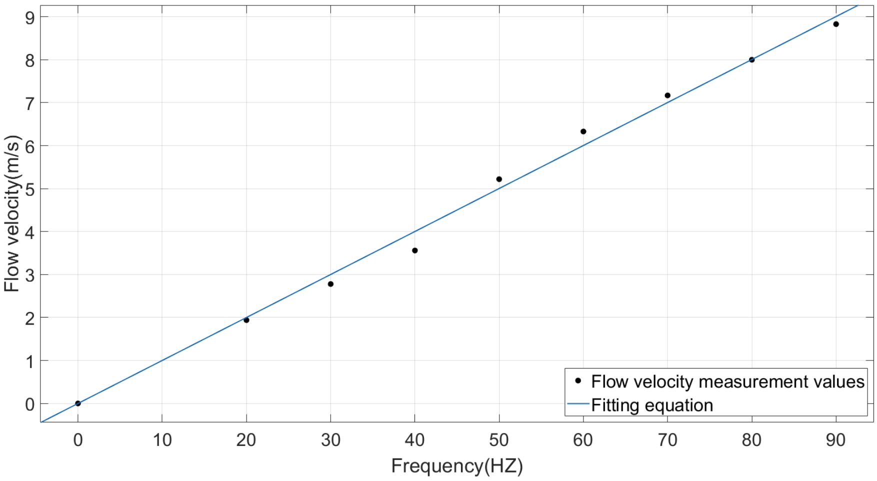

Figure 4.17: Propeller flow velocity fitting with matlab

The equation is

$$v = F \times 0.09286 \tag{4.4}$$

After preparing all the experimental equipment, the real experimental setup is shown in (Fig. 4.18). The sensor is fixed in front of the propeller, the two have the same height, 50 mm apart.

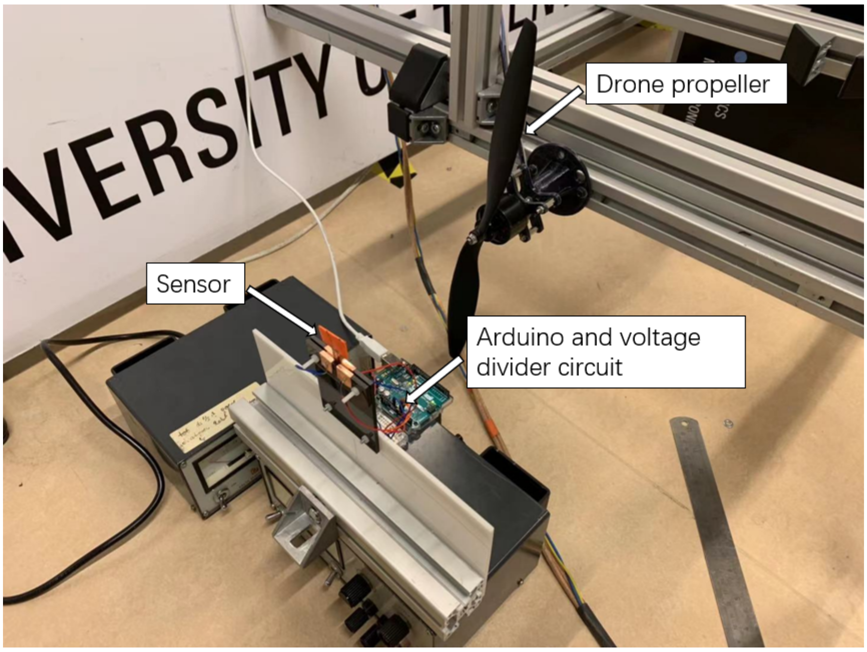

Figure 4.18: Real experiment setup of control system experiment

4.6.2 Experiment plan

According to the design in Chapter 2, the experiment mainly explores whether the feedback loop composed of sensors can play a role in the control system, and study its working characteristics.

Constant reference

First, the reference of the control system will be set to a constant value, and the operation of the entire system will be observed. For example, the system output (motor flow velocity) is whether and how fast can stabilize at the reference value. In addition, the role of the sensor in the control system is also an important object of investigation.

Sine wave reference

For the changing reference, this experiment is planned to use a slowly changing sine signal. The main observation is whether the control system can maintain good tracking of the reference under the feedback of the sensor.

Theoretical analysis in Simulink

After the experiment, some analysis work will be carried out through simulation in Simulink.

The block diagram of the model in simulink is shown in (Fig. 4.19). First, a sensor model is made as a second-order system by the dynamic analysis from Chapter 2, which is the sensor block in the figure. Then, an ideal motor model is obtained by the calibration of the drone propeller in chapter 4, which is motor block in the figure. In addition, the reference and PI controller block in the figure represent the same components as the previous experiment. The PC block represents the process of using Arduino to receive sensor signals. In this process, the resistance change signal is converted to flow velocity, and it contains a low-pass filter(second order Butterworth filter) with a cut-off frequency of 5 Hz.

In addition, according to the actual situation in the experiment, the output of the motor has some delay compared with the control signal, as shown in the delay block in the figure. And,in the program that controls the drone propeller, for safety reasons, the minimum output flow velocity of the propeller is $1.5\,\mathrm{m\,s^{-1}}$, so a saturation block is added after the motor.

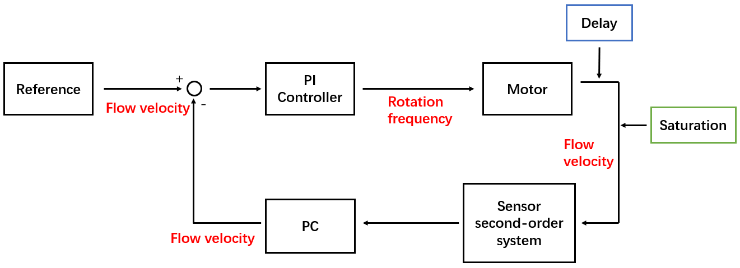

Figure 4.19: Block diagram of theoretical analysis in Simulink

4.7 Conclusion

This chapter focuses on the experimental principles and measurement set-ups in this project. The results of these experiments and applications will be presented and analyzed in the next chapter.

5 Experimental Results

5.1 Introduction

This chapter will introduce all the experimental results and some brief analysis. They include the results of initial experiments, sensor characterization, dynamic analysis, wind tunnel experiments and control system experiments.

5.2 Results of initial experiment

From chapter 3, the model 6 should be the best design, but this judgment requires experimental verification. This experiment tested all 14 sensors, all of them were placed in the same set-up. At the begin of all tests there is no air flow, then the flow appear which flow velocity is 8.3 m/s, after a while the flow disappear again. The experimental results are mainly analyzed from two aspects, namely the degree of resistance change and the degree of stability of the measured signal. Stability indicates the fluctuation range of the measurement signal after the outside airflow is stable. Part of the experimental results are shown in table 5.1 below.

Number	Type	Maximum change in resistance(Ω)	Stability of measurement signal
0	model 2	0	Thickness too thin: resistances on both sides shorted.
1	model 2	30	Unstable
2	model 2	30	Unstable
3	model 2	0	The thickness is too large to produce effective deformation.
4	model 2	0	The thickness is too large to produce effective deformation.
5	model 3	40	Unstable
6	model 3	40	Unstable
7	model 3	40	Unstable
8	model 4	40	Very unstable
9	model 4	40	Very unstable
10	model 5	30	Stable.
11	model 5	30	Stable.
12	model 6	50	Very stable
13	model 6	60	Very stable

Table 5.1: Results of initial experiment

In addition, the details of the experimental results of each sensor are introduced. First of all, for sensor 0, its thickness is too thin, causing the strain gauges on both sides to be connected and unusable.

The next measurement is sensor 1 and 2. They are thicker than sensor 0 and they all use model 1 design. The results show that their resistance changes are small and not stable.

Sensors 3 and 4 are still printed with model 2 the same as the previous sensors, but their thickness is the largest. Through experiments, the thickness of sensor 3 and sensor 4 is too large. At the same flow velocity, there is basically no deformation, and the resistance is basically unchanged, so they are not available for subsequent experiments.

Sensors 5, 6 and 7 are printed according to model 3, which are enlarged versions of the previous sensors. Sensor 5 has a smaller thickness than sensors 6 and 7. From the experimental results, their resistance changes are greater than those of small sensors, but the signal is very unstable. The bottom connection parts of the big sensors are very large, which causes them to be unstable when they are fixed to the experimental set-up. Even after the surface of its connection part is coated with silver paint, its measurement signal is still unstable.

Sensor 8 and 9 are printed according to model 4. Model 4 added a support part to eliminate the difference in roughness between the two sides of the sensor. But judging from the print results, this support part can not solve the problem, and the side close to the printer glass is still smoother. Therefore, the results of sensors 8 and 9 are actually similar to those of sensors 5, 6 and 7.

In addition, all large sensors have a common problem, that is, the resistance of the strain gauges on their rough surface is very insensitive, especially when the strain gauge is compressed. There is basically no change in resistance, but the smooth surface of the strain gauge is very sensitive. This is different for the small sensors.

Sensors 10 and 11 use exactly the same design printed according to model 5. Model 5 is an improved version of model 2. The results are similar to sensor 1 and 2, and the improvement is that the measurement signal is more stable. That because the silver paint improve the quality of connection points.

The last to be measured are sensors 12 and 13, which are printed according to model 6. Under the same airflow, they produced the largest resistance change, and this change is very stable. The experimental results of sensor 12 and sensor 13 on both sides are shown in (Fig. 5.1), (Fig. 5.2), (Fig. 5.3), and (Fig. 5.3). The counts in the picture represent the samples. The sampling frequency of the experiment is 50 HZ, so there are 50 counts per second.

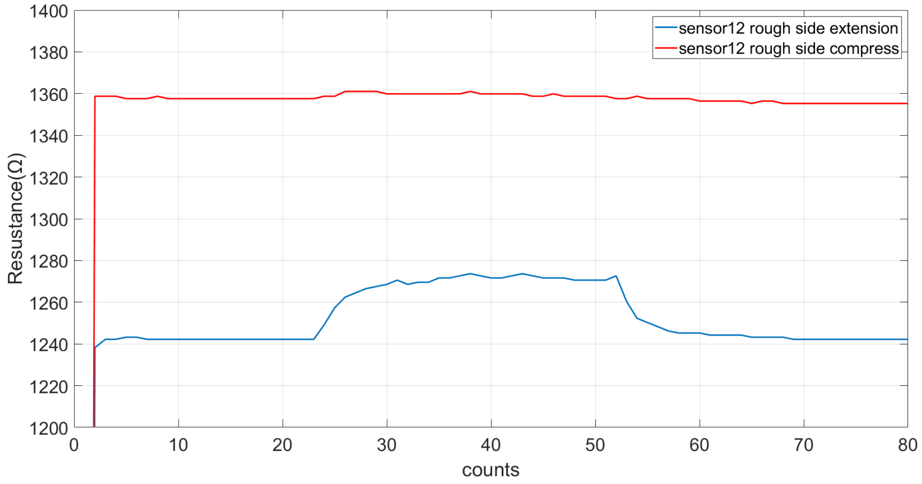

Figure 5.1: sensor 12 rough side initial experiment results

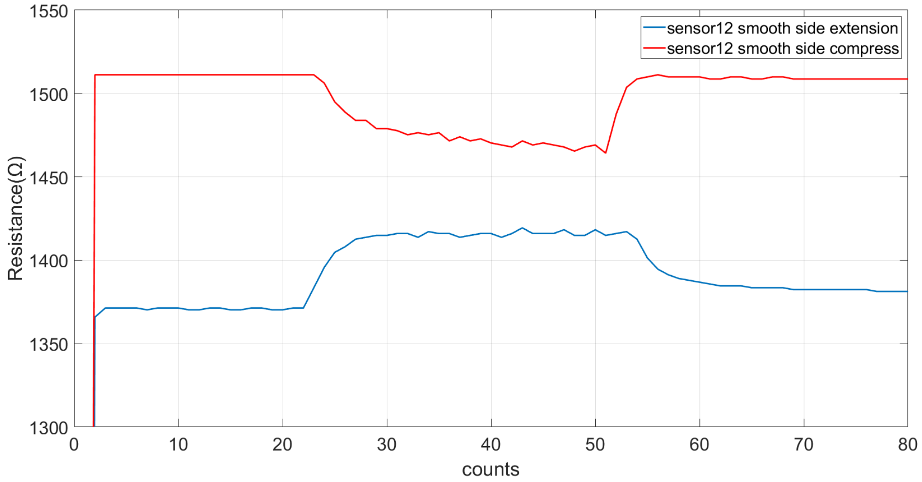

Figure 5.2: sensor 12 smooth side initial experiment results

In these figures, the extension indicates that this side is close to the airflow source, and the strain gauge is stretched. Compress indicates that this side is away from the airflow source, and the length of the strain gauge is compressed. The initial resistance of the same surface is different because the connect point between the sensor and the set-up is different in two experiments.

From the above two pictures, we can see from the overall results that sensor 12 performed well. Only the compression result on the rough side is not good. Its two sides basically behave the same when stretched. The large difference in steady resistance is because of the connection position is changed during the experiments.

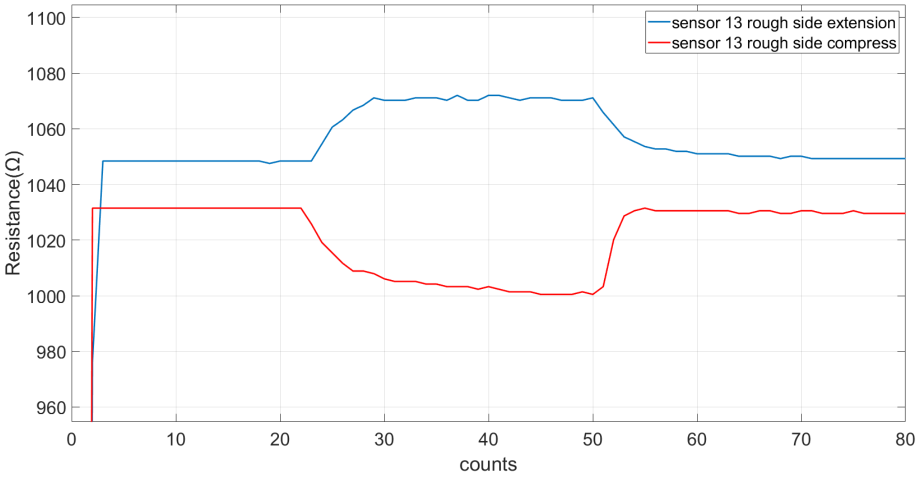

Figure 5.3: sensor 13 rough side initial experiment results

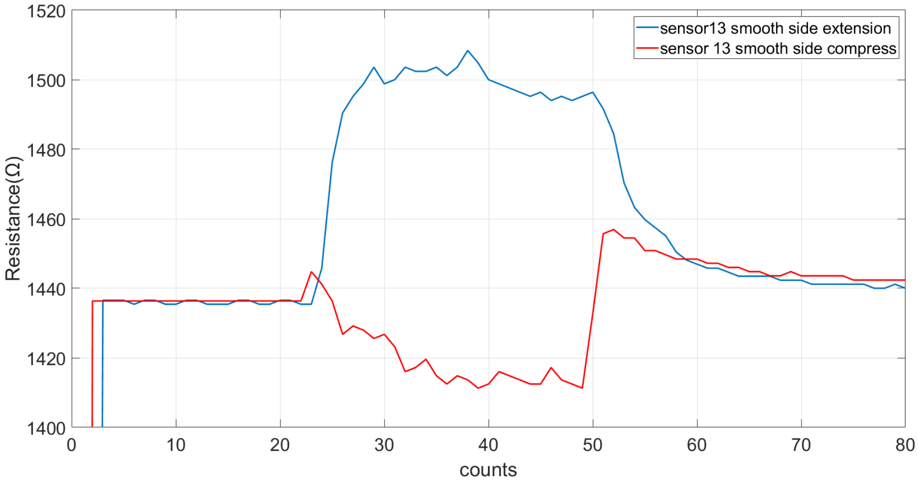

Figure 5.4: sensor 13 smooth side initial experiment results

It can be seen from the experimental results that the performance of sensor 13 is very good. The resistance on both sides decrease about 30 Ω when compressed. When being stretched, the resistance of the smooth side changes even more at about 60 Ω. The resistance of a smooth surface is always greater than that of a rough surface, and when the sensor is stretched, the change in resistance is more obvious than when it is compressed.

In addition, from these results, E-TPU has the tendency to reduce resistance on initial strain, turning over to increasing resistance at larger strain. This shows that this material needs a certain amount of time to reach a stable resistance change, and in the long-term deformation, it will produce drift, thereby continuously increasing the measured value.

Overall, sensor 13 has the best experimental results. Its two sides have the same basic characteristics in the experiment. Under the same airflow, it has the largest resistance change and most stable measurement signal. Therefore, sensor 13 was selected for subsequent experiments.

5.3 Results of mechanical sensor characterization

5.3.1 Measurement

According to the previous analysis, sensor 13 has the best performance. So the experiment started with sensor 13 and the voltage changes of the strain gauges on both sides of it are shown in (Fig. 5.5) and (Fig. 5.6). In addition, the displacement of the SMAC header that produces this voltage change is shown in (Fig. 5.7). In this experiment, the power supply voltage is set to 10 V, the measurement time is 100 s, and the SMAC excitation frequency is 0.5 Hz.

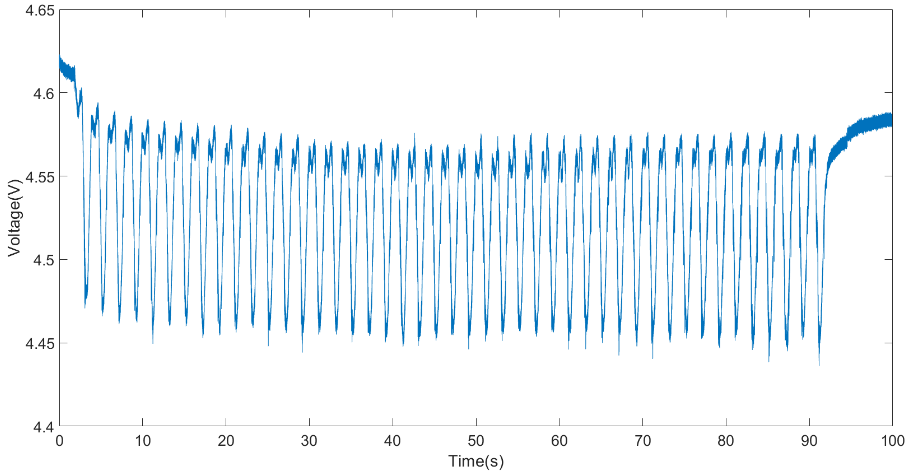

Figure 5.5: Sensor-1

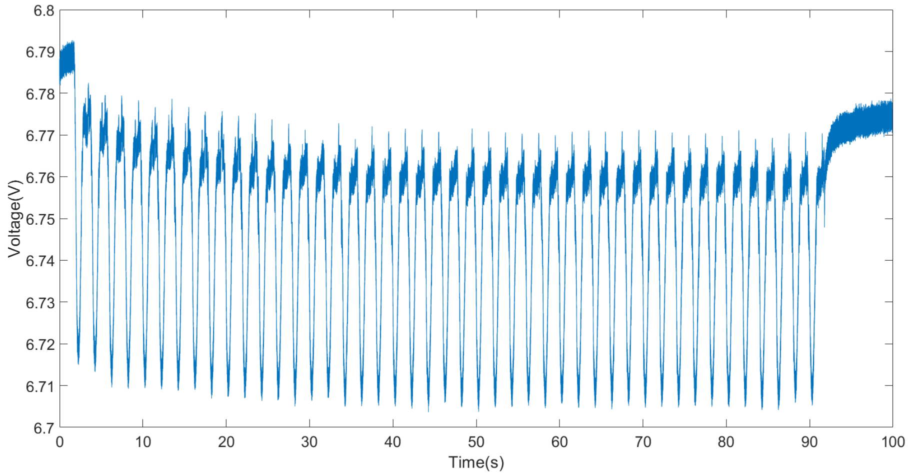

Figure 5.6: Sensor-2

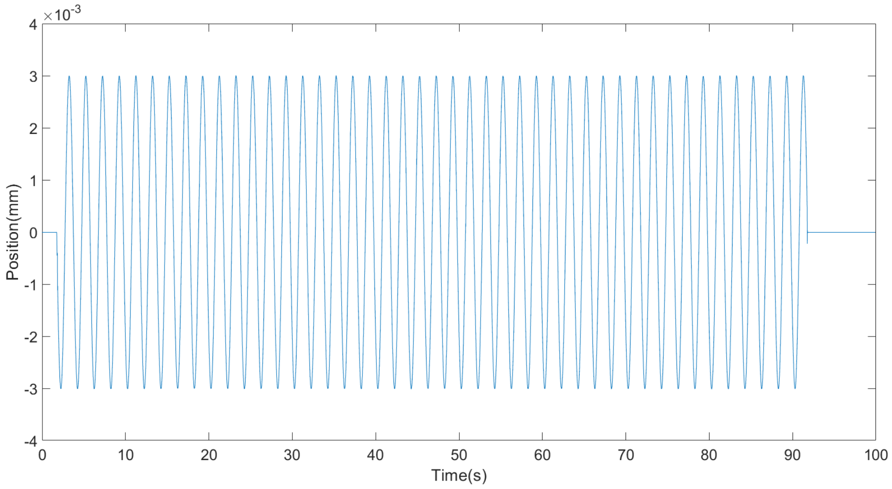

Figure 5.7: SMAC head displacement

In order to reduce the noise in the experimental results, we need to analyze this voltage change in the frequency domain. The FFT transform of the voltage changes of the strain gauges on both sides of sensor 13 are shown in (Fig. 5.8).

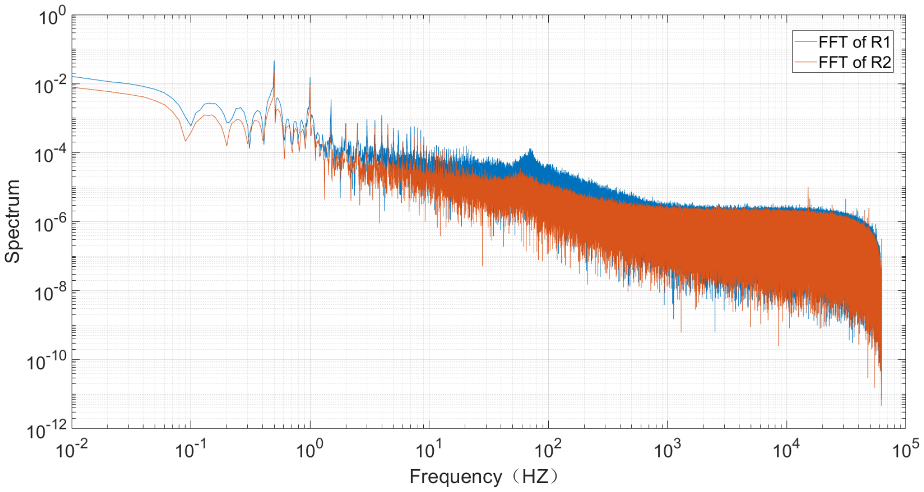

Figure 5.8: Frequency spectra of the output voltages of R1 and R2 when excited by the SMAC with a frequency of 0.5 Hz.

According to the experimental circuit diagram designed above, the voltage change of the strain gauges on the sensor can be converted into the changes in resistance of R1 and R2. The result is shown in (Fig. 5.9).

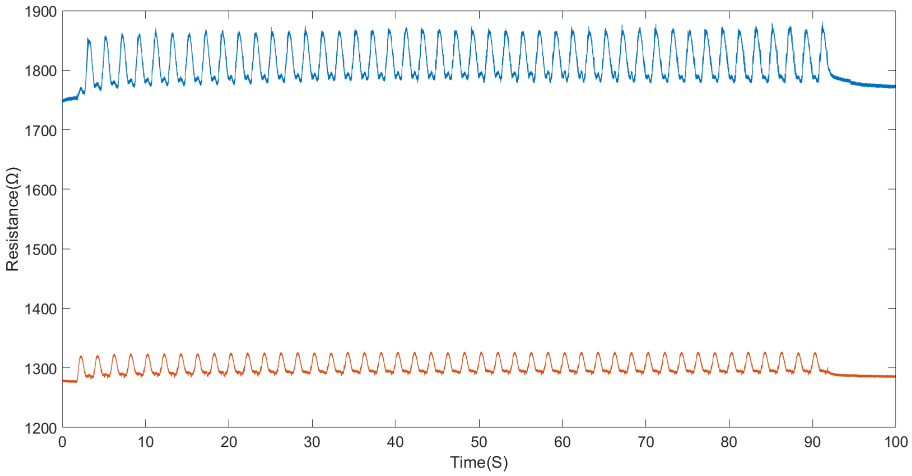

Figure 5.9: The change in R1 and R2.

After the above frequency domain analysis, the model can be processed with a low-pass filter(second order Butterworth filter) of 5 Hz cut-off frequency, and the difference between R1 and R2 after processing is shown in (Fig. 5.10).

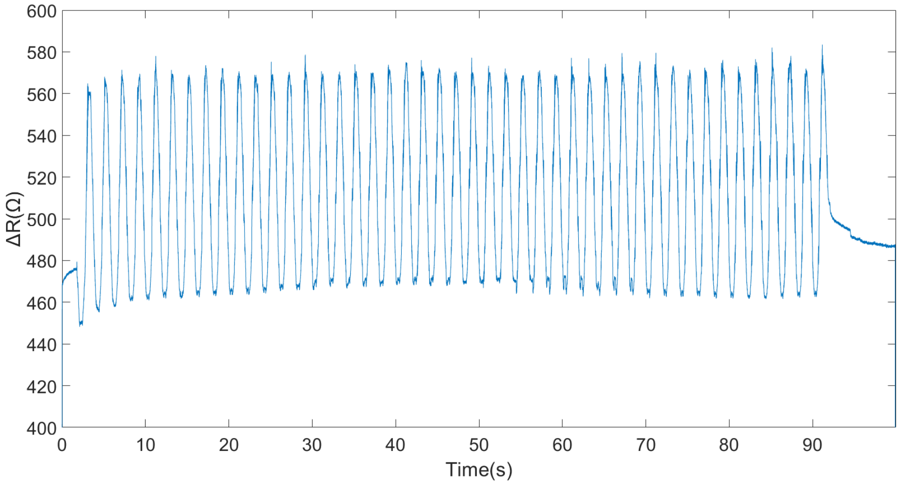

Figure 5.10: The differential of R1 and R2 with 5 Hz low pass filter.

5.3.2 Results

From the calculation in Chapter 2, ΔR/R and ΔL/L can be obtained. ΔR/R is shown in (Fig. 5.11). And, ΔL/L is shown in (Fig. 5.12).

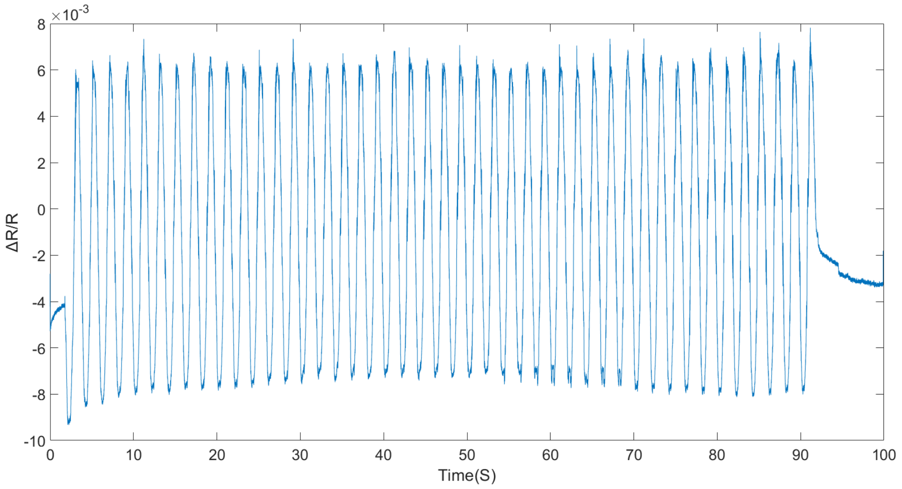

Figure 5.11: The relative change in resistance.

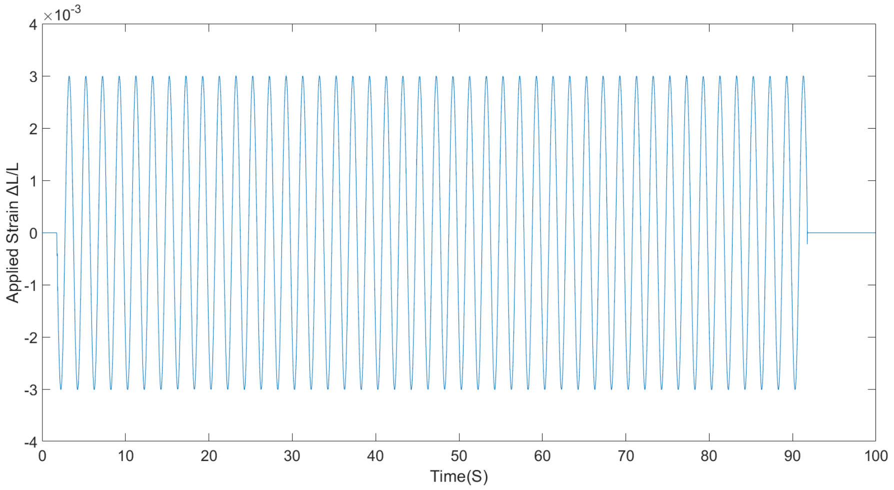

Figure 5.12: The relative change in the combined strain.

The relationship of $\Delta R/R$ and $\Delta L/L$ is shown in (Fig. 5.13).

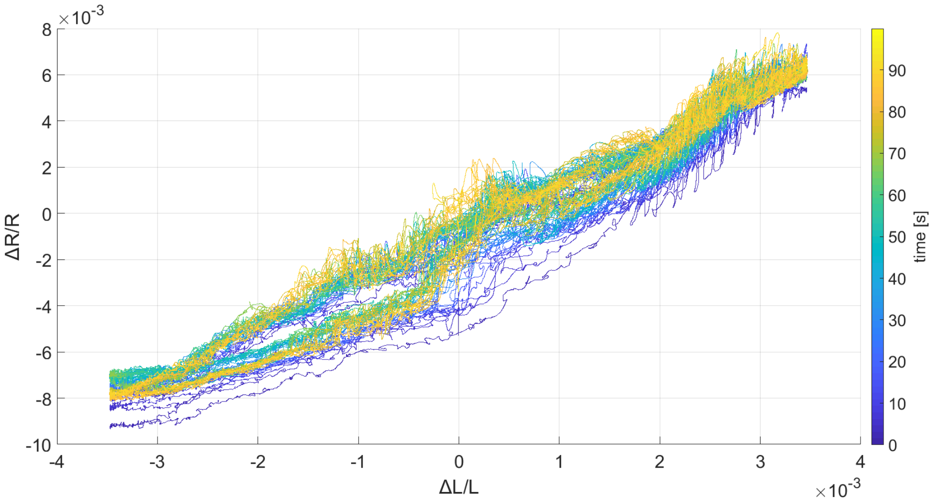

Figure 5.13: The differential relative change in resistance(ΔR/R) with respect to the applied strain(ΔL/L) and time with 5 Hz low pass filter.

The results in (Fig 5.13) show that there is some non-linearity and hysteresis between ΔL/L and ΔR/R. But the overall trend between these two is still roughly linear. In addition, according to the different times represented by different colors in the figure, the relationship between ΔL/L and ΔR/R produced obvious drift during the experiment, and it continued to increase over time.

Approximation

In order to facilitate the calculation of the conversion from $\Delta R/R$ to $\Delta L/L$, an approximate linear relationship must be found. By taking the average magnitude of the applied strain and dividing it by the average magnitude of the resistivity $\Delta R/R$ an approximation factor $\alpha = 0.4363$ has been found. An approximation of the strain (orange) with α together with the applied strain(blue) is shown in (Fig. 5.14).

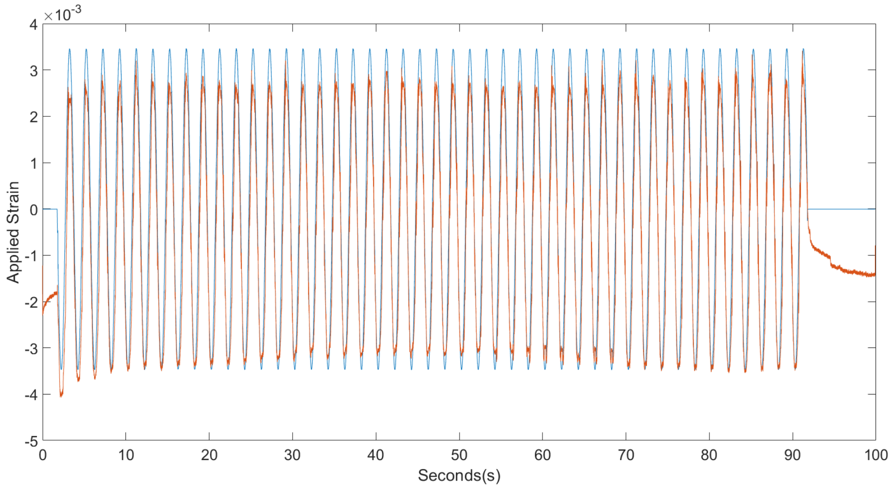

Figure 5.14: An approximation of the strain (orange) with $\alpha = 0.4363$ together with the applied strain (blue).

From the result point of view, this approximation roughly meets the demand, and there are some errors. When the sensor is not deformed, there is a big gap between the actual value of apply strain $\Delta L/L$ and the approximate value.

5.3.3 Conclusion of mechanical sensor characterization

According to the above experimental results, it can be seen that there is some hysteresis and drift between the strain gauge deformation and the resistance change of the sensor. A factor α can be obtained to approximate the relationship between resistance and deformation. This is very important for the subsequent application of the sensor, although this approximation is not completely accurate.

5.4 Results of dynamic analysis

According to the content of Chapter 4, the shaker experimental system can make the sensor vibrate at different output frequencies to obtain the eigenfrequency of the sensor. This result can be compared with the model result analyzed previously. And this data can be applied to the improvement of the control system. The frequency spectrum of sensor 12 and sensor 13 is shown in (Fig. 5.15). In this experiment, the sampling frequency is 5000 Hz and the duration is 60 s for both sensors 12 and 13.

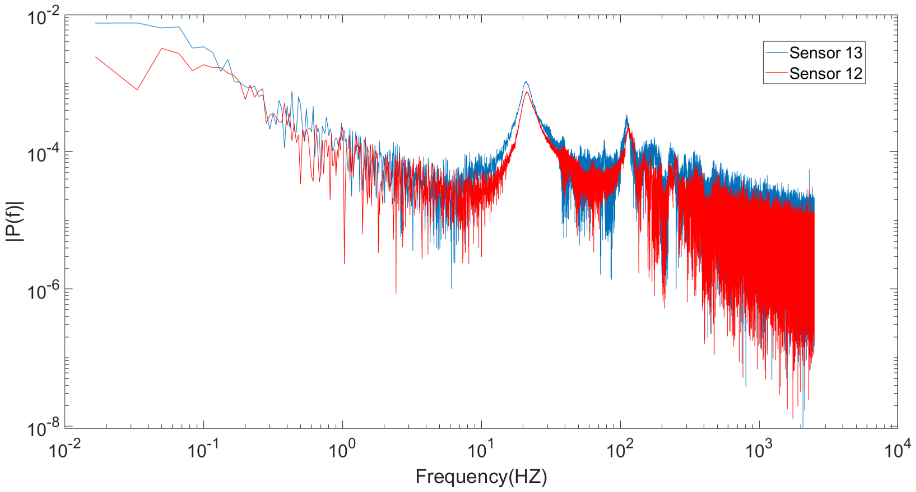

Figure 5.15: Bode plot of sensor 13 and sensor 12

As can be seen from the figure, the results of sensor 12 and sensor 13 are very similar. This is expected, because sensor 12 and sensor 13 use the same design. This proves from another aspect that the results of this experiment are basically reliable and it also shows that the printing has a certain degree of repeatability.

From the results , the eigenfrequency(f_n) is around 20 Hz, and quality factor(Q) is around 10. After some experiments, the cutoff frequency of the low-pass filter((second order Butterworth filter) is set to 5 Hz, the noise in the system can be better eliminated.

Next, compare this result with the dynamic model in Chapter 2. According to the equation (2.4), the frequency response of the system can be known. From the parameter in Chapter 3, the volume of sensor 13 can be known, and the density of sensor should be around 1.3 g/cm^3 [24]. Then the results can be obtained that f_n=17.5 Hz which has some difference from the results(20 Hz) of experiment. This result proves that the dynamic model in Chapter 2 has some errors, but not very big. However, since sensor 13 does not fully meet all the conditions of the pseudo-rigid-body approximation, it is normal for some deviations.

In addition, according to equation (2.23) in Chapter 2, the damping factor(ζ) of the system is 0.05. From [25], if the ζ of the system is: $0 < \zeta < 1$, the system will be in an underdamped state, which may also affect the subsequent experimental results.

In summary, according to the experimental results and dynamic model analysis, it is decided to set the cut-off frequency of the system's low-pass filter to 5 Hz. And the sensor system may have the problem of under-damping.

5.5 Results of experiment with wind tunnel

5.5.1 Constant flow

As mentioned in Chapter 4, the first experiment is to place sensor 13 in various constant air flows to measure and observe the actual performance of the sensor. The experimental results are shown in (Fig. 5.16). The experiment starts from $2\,\mathrm{m\,s^{-1}}$ with an increase of $1\,\mathrm{m\,s^{-1}}$ and the maximum value is $10\,\mathrm{m\,s^{-1}}$.

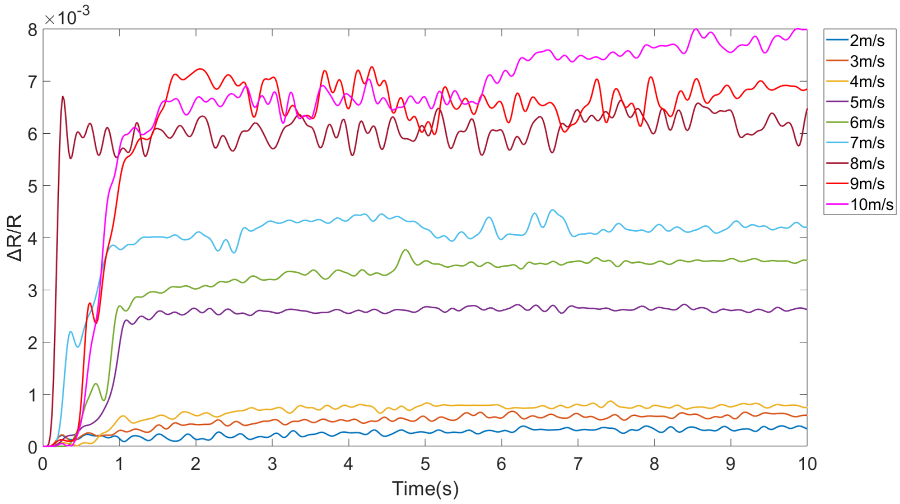

Figure 5.16: Sensor measured data at different flow velocity setpoint in wind tunnel

The rising part of the curve in the figure indicates that the airflow in the wind tunnel will be opened after a short period of time after the start of the experiment. This result shows that the best measurement range of sensor 13 is about $2\,\mathrm{m\,s^{-1}}$ to $7\,\mathrm{m\,s^{-1}}$. When the flow velocity is too large, the measurement signal of the sensor becomes more and more unstable. This situation comes from the vibration of the sensor under a large flow velocity which can be observed from experiment. When the flow velocity in the wind tunnel is relatively large, turbulence will be generated around the sensor due to the interaction between the flow and the sensor [26]. In combination with the very flexible beam, the oscillations observed are aero-elastic effects due to the fluid-structure interaction.

Compared with the initial experiment, the airflow in the wind tunnel is more stable which can basically be regarded as a steady laminar flow, and the displayed number on its screen is closer to the real airflow velocity. Therefore, the experiment data is used to compare with the equation(2.9) for proving the correctness of the calculation.

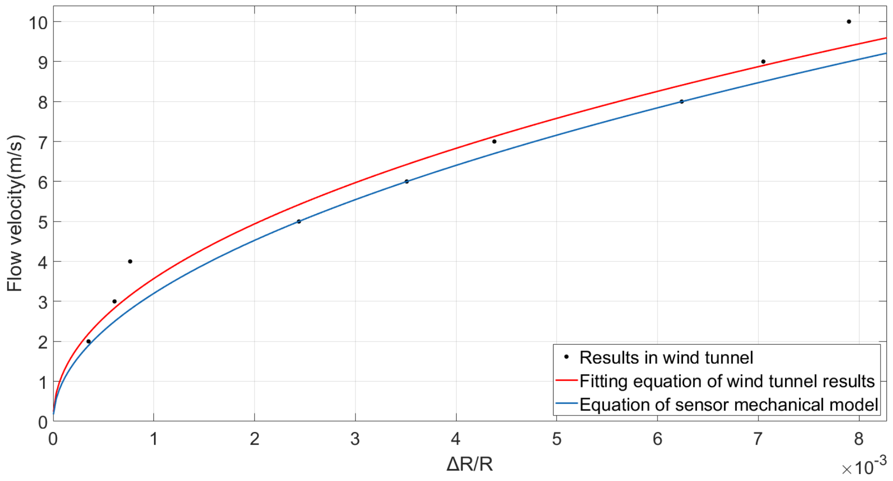

Figure 5.17: Comparison of sensor mechanical model and wind tunnel results

The result is somewhat different from the sensor mechanical model equation (2.9), but the difference is not very big. It can be proved that the calculation results in Chapter 2 are desirable.

5.5.2 Step change test

This experiment will make the flow velocity in wind tunnel start from $0\,\mathrm{m\,s^{-1}}$ and increase $2\,\mathrm{m\,s^{-1}}$ every ten seconds to $10\,\mathrm{m\,s^{-1}}$ and then decrease back to $0\,\mathrm{m\,s^{-1}}$ at the same speed.

Based on this result, the average and standard deviation of the sensor measurement values under the same flow velocity every ten seconds are obtained. The mainly MATLAB code using for data processing is shown in appendix A.

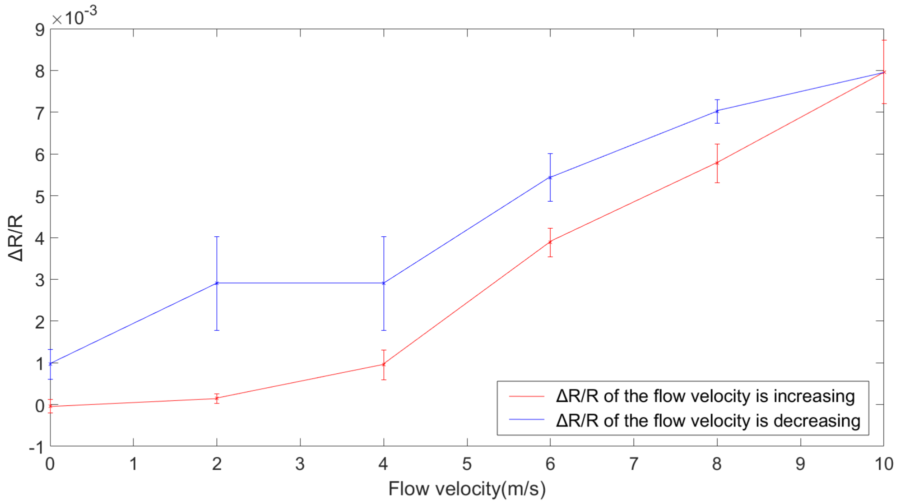

Figure 5.18: In the wind tunnel step change experiment, the average and standard deviation of sensor measurement values corresponding to different flow velocities.

It can be seen from the figure 5.18 that when the flow velocity in the wind tunnel is reduced step by step, the measured values are always greater than when the flow velocity is increased step by step. Therefore, there must be some drift in the sensor when the flow velocity is decreasing. And this drift also gives rise to hysteresis which leads to the non-linearity of the sensor measurement.

5.6 Results of control system experiment

This part of the report will show the results of the control system experiment. It mainly includes the parameter adjustment of the PI controller, the experimental results for the case of a constant reference, the experimental results for the case of a sine wave reference and the experimental results of the control system when it only contains a feedback loop.

5.6.1 Calibration for sensor 13

In order to verify the correctness of the relationship equation (2.9) between sensor deformation and flow velocity in Chapter 2, sensor 13 needs to be calibrated first.

The sensor 13 is fixed at the same height as the drone propeller and a distance of 50 mm, and the propeller's rotation frequency increase from 20 Hz to 90 Hz. According to the equation(2.9) in Chapter 2, the corresponding air flow velocity can be calculated. Then a linear fitting equation will also be obtained by Matlab. Finally, this equation is compared with the calibration of drone propeller in Chapter 4. All these results are shown in (Fig. 5.19).

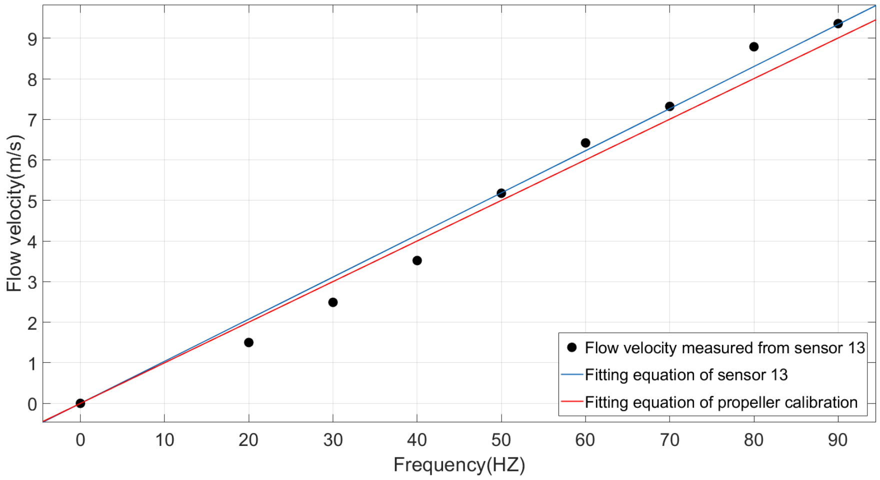

Figure 5.19: Calibration of sensor 13 compare to the calibration of drone propeller

In this picture, the black spots represent the values which the measurement data use equation(2.9) transform to flow velocity. Then, the blue line represents their linear fit curve. And the red line is calibration of drone propeller. It is obvious that there are only small differences between sensor measured values and actual flow velocity. This proves that the equation(2.9) in Chapter 2 is credible, and it basically reflects the relationship between sensor deformation and flow velocity.

5.6.2 Controller parameter tuning

The first display is the experimental results of the PI controller parameter adjustment. First, based on experience, in the experiment, p=0.5 and i=0.5 is chosen to start. After that, the values of the two parameters will be adjusted step by step, and the best combination will be selected by comparing the results. In each parameter tuning experiment the noise is set to 0.

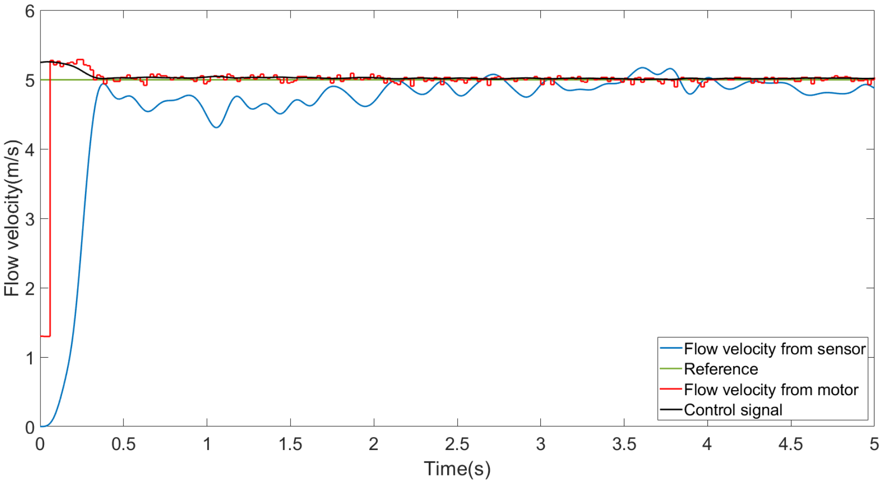

Figure 5.20: p=0.5 i=0.5 with constant reference 5 m s^{-1}

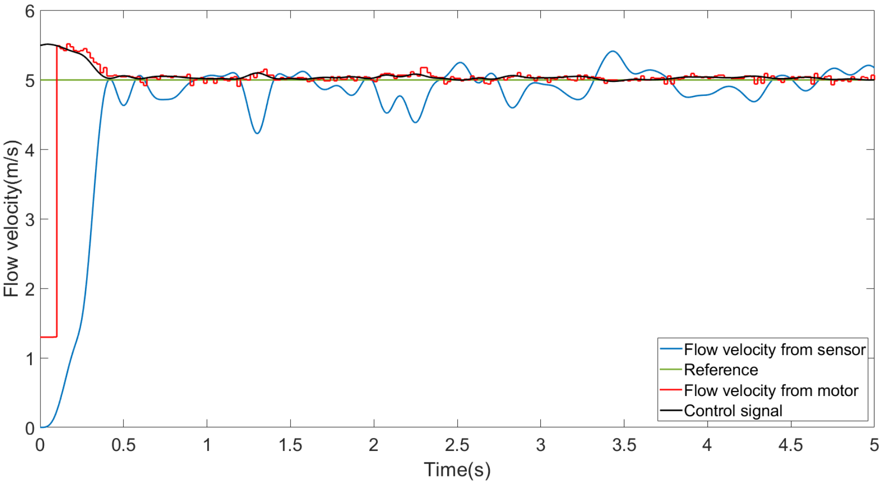

Figure 5.21: p=1 i=1 with constant reference 5 m s^{-1}

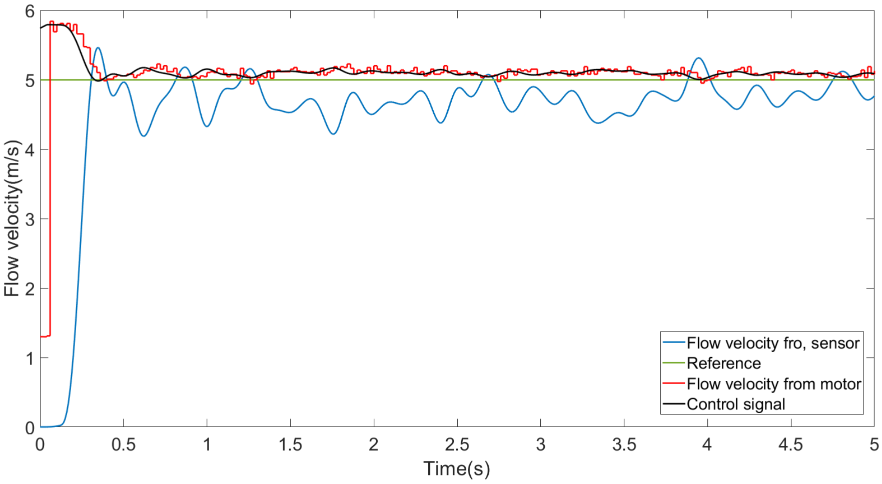

Figure 5.22: p=1.5 i=2.6 with constant reference 5 m s^{-1}

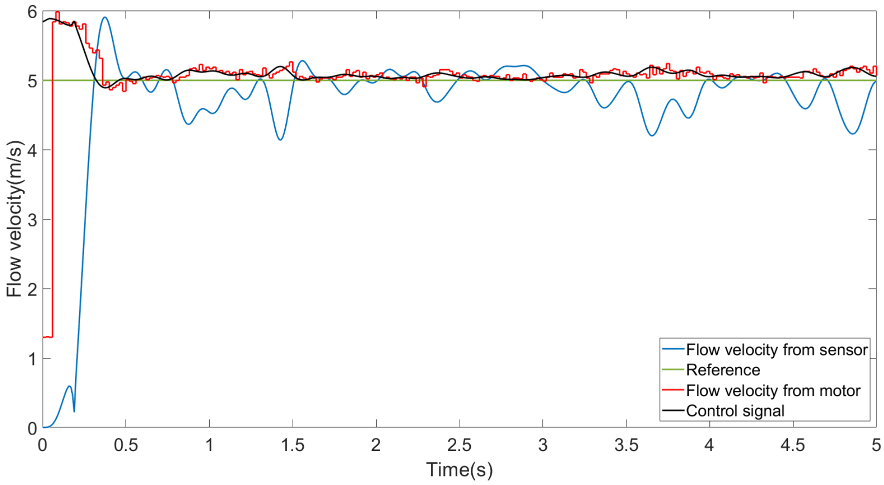

Figure 5.23: p=1.7 i=2.6 with constant reference 5 $\mathrm{m\,s^{-1}}$

In general, according to experimental results, the greater the value of p, the greater the fluctuation of the control signal and the measured value, the greater the value of i, the slower the system will reach stability. But when the values of p and i are too small, only the feed-forward loop is working, and the controller does not influence the control signal. So two suitable values, p=1.5, i=2.6 are selected.

5.6.3 Constant reference

As mentioned earlier in the article, the first thing to be shown are the experimental results under constant reference. The experimental result with a reference of 5 $\mathrm{m\,s^{-1}}$ is shown in (Fig. 5.24). For safety considerations, first experiment set the value of noise to 0. From the previous analysis, the best PI controller parameters are p=1.5 and i=2.6. The red line is the actual output flow velocity of the propeller, the blue line is the flow velocity value measured by the flow sensor, and the green line is the constant reference at 5 $\mathrm{m\,s^{-1}}$. The black line represents the control signal from the controller.

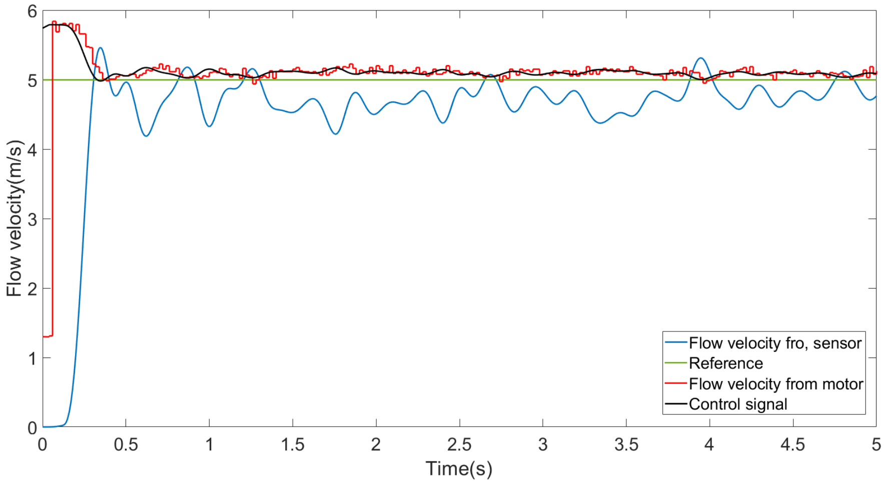

Figure 5.24: Control system experiment results with constant reference 5 $\mathrm{m\,s^{-1}}$

According to the experimental results, it can be seen that the control system works well because the motor flow velocity quickly stabilizes at the reference value. The flow velocity of the motor basically matches the control signal. However, the sensor's contribution to the entire control system is limited. It can be seen from the figure that there are some not very obvious mirror fluctuations between the sensor value and the control signal. This shows that the feedback loop in which the sensor is located has a certain effect on the common work of the control system but it is very limited. In addition, the measured value of the sensor first reaches the reference at 0.3 s.

Next, the standard deviation of the white noise is set to 0.15 to observe whether the effect on the control signal of the sensor will be improved.

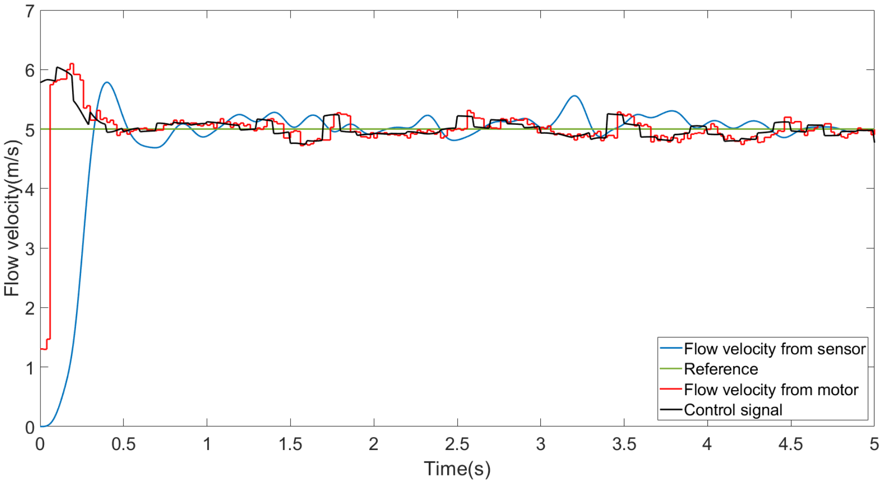

Figure 5.25: Control system experiment results with constant reference 5 $\mathrm{m\,s^{-1}}$ and white noise

It can be clearly seen from (Fig. 5.25) that after noise is added to the feed forward loop of the control system, the control signal and motor flow velocity become more unstable. They all have some jagged ups and downs. However, compared with the result without noise, the working proportion of the sensor has not been greatly improved. Overall, in these two experiments, the sensor is almost not working for the control system.

5.6.4 Sine wave reference

The second part of the experiment will set the reference to a sine wave. Because the minimum flow velocity that can be produced by the propeller is about 1.5 $\mathrm{m\,s^{-1}}$, and for safety reasons, its maximum speed should not exceed 6 $\mathrm{m\,s^{-1}}$. Therefore, in this experiment, its amplitude is 2 $\mathrm{m\,s^{-1}}$ and the frequency is 0.08 Hz and starts from 3.5 $\mathrm{m\,s^{-1}}$. The results are shown in (Fig. 5.26)

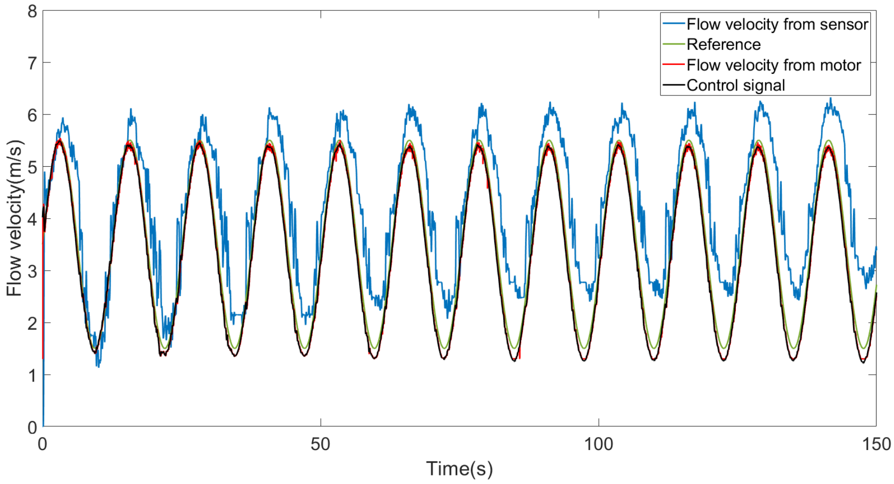

Figure 5.26: Control system experiment results with sine wave reference

It can be seen from the figure that the control system works normally and the motor flow velocity is in good agreement with the control signal because of the prefect feed-forward loop. However, the measured value of the sensor is very different from the control signal. In the initial stage of the experiment, the sensor performed well, but as time passed, the drift in the sensor gradually increased, and it gradually could not measure the accurate flow velocity. The measured value of the sensor is obviously greater than the actual flow velocity and the gap is getting bigger and bigger.

This measurement error originates from drift caused by long-term sensor deformation. In the experiment, as time increases, the drift in the sensor continues to expand, so its measured value deviates further and further from the actual value. This shows that this flow sensor is not suitable for long-term quantitative measurement work.

5.6.5 Only feedback control

Next, in order to further explore the working ability of the sensor under constant reference, the feed-forward loop of the control system is switched off. The control system will depend to the greatest extent on the measured value of the sensor to work. The results are shown in (Fig. 5.27).

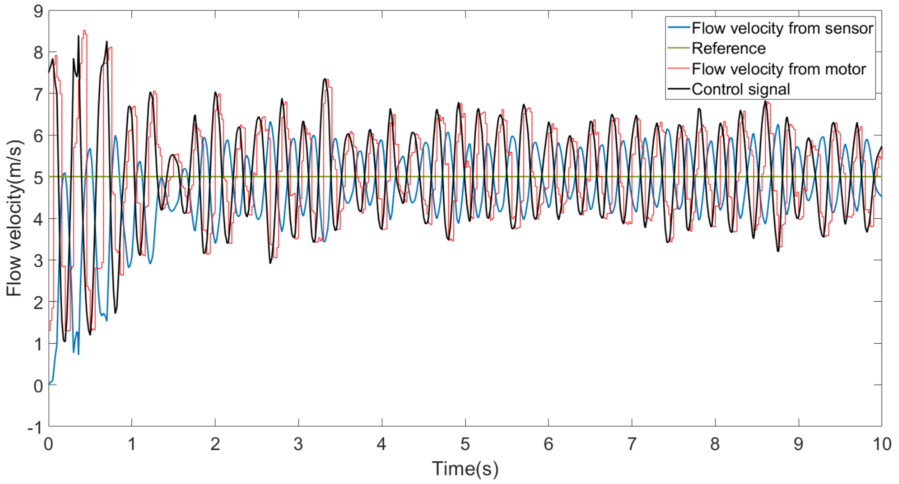

Figure 5.27: Constant reference at 5 $\mathrm{m\,s^{-1}}$ without feed-forward loop

It can be clearly seen from the results that the control system can not work well. The sensor's measured value, control signal, and motor's output are constantly vibrating around the reference and cannot be stabilized. According to the dynamic analysis of the sensor in Chapter 2 and the dynamic experiment results in Chapter 5, it is highly likely that the under-damping causes the problems.

In order to deal with the fluctuation problem of this system, the cut-off frequency of the low-pass filter in the control loop is reduced. The corresponding results for several different cut-off frequencies are shown in (Fig 5.28).

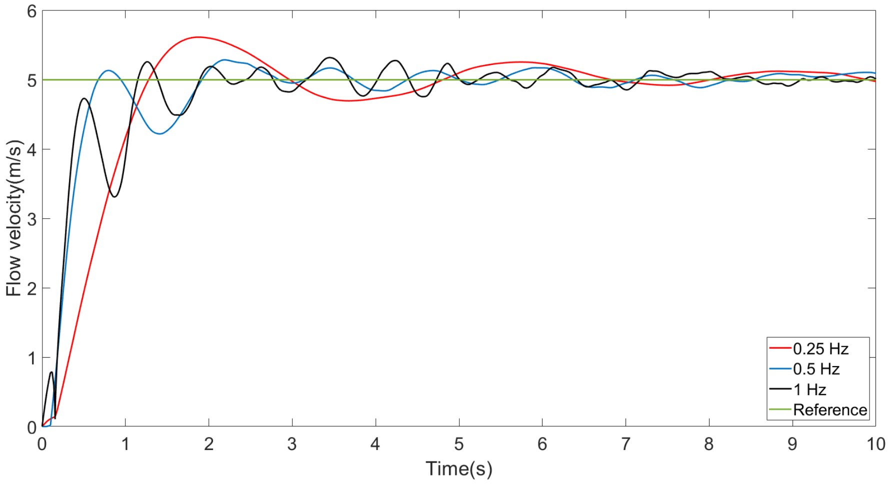

Figure 5.28: Comparison of the flow sensor measurement results with several different cut-off frequencies.

From the results, it can be judged that 0.5 Hz has the best control result. Its measured value of the flow sensor reaches the reference first and stabilize the fastest. Therefore, the cut-off frequency of the low-pass filter is selected as 0.5 Hz, and the experimental results of the overall control system are shown in (Fig 5.29).

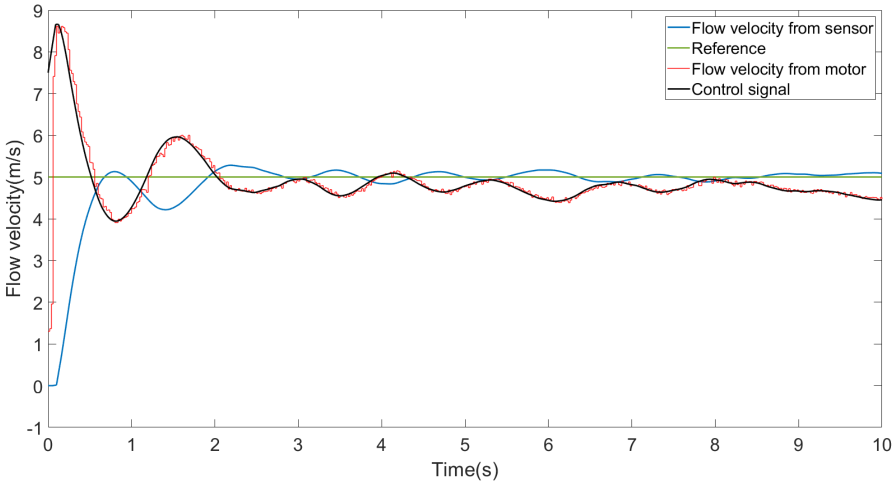

Figure 5.29: Constant reference at 5 m s^{-1} without feed-forward loop and the low pass filter cut-off frequency is 0.5 Hz

The result shows that the control system works and the previous instability problem is improved. This shows that this flow sensor can work in this PI closed-loop control system. However, because the cut-off frequency of the system is very small, the entire system becomes very slow.

5.6.6 Theoretical analysis in Simulink

In the previous section, the system showes some problems in the experiment of only feedback loop. This part will further analyze these issues through simulation in Simulink, and suggest solutions.

Then, according to the previous analysis of the control system not working properly, the main problem seems to be the under-damping problem of the sensor. Therefore, according to the simulation block diagram in Chapter 4, all important parameters in the simulation are showing:

- Controller parameter: p=1.5; i=2.6.
- Delay of the motor: 0.015 s.
- Sensor second-order system: f_n=20 Hz, Q=10;
- Saturation of motor=lower bound of 1.5 $\mathrm{m\,s^{-1}}$ and upper bound of 10 $\mathrm{m\,s^{-1}}$.

For a better comparison, the simulation results with a ideal sensor model and no delay and saturation are shown first in (Fig 5.30). Then the simulation result with second-order system and delay and saturation is shown in (Fig 5.31).

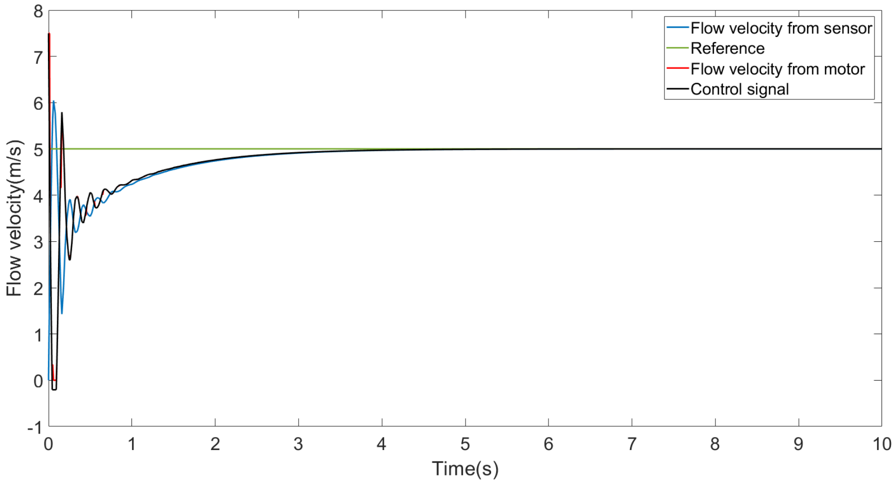

Figure 5.30: The simulation results of the ideal sensor model without delay and saturation

The result of (Fig 5.30) is a typical normal PI control system working condition. The ideal sensor model has good working ability and it can help the motor flow velocity to follow the reference well.

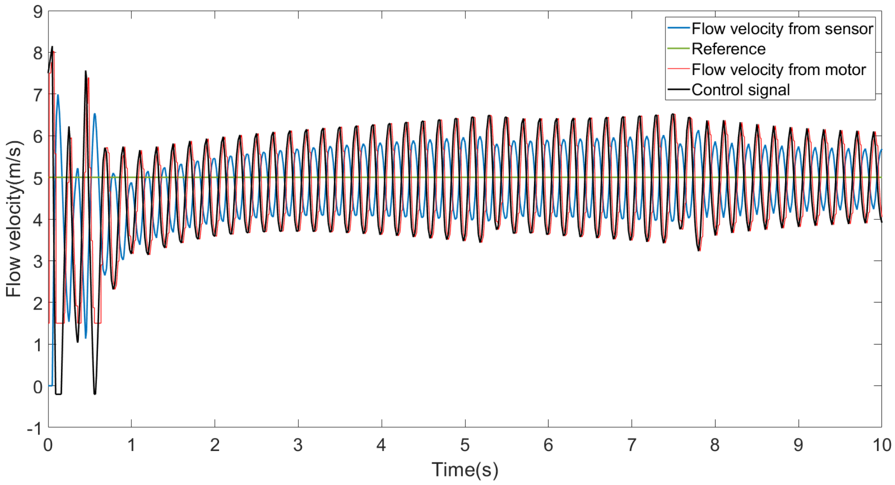

Figure 5.31: Simulation results with a second order system

The results show that this second-order system can simulate the problems in the experiment very well. This also shows that the problem of signal instability in the control system may comes from the under-damping of the sensor.

In order to cope with this problem and improve the working ability of the control system, velocity feedback control was used in Simulink. According to the introduction in Chapter 2, K_t is set to 0.087 and a plant of $K_t(s)$ is made in Slimulink, then the block diagram of the new model is shown in (Fig 5.32). The results are shown in (Fig 5.33).

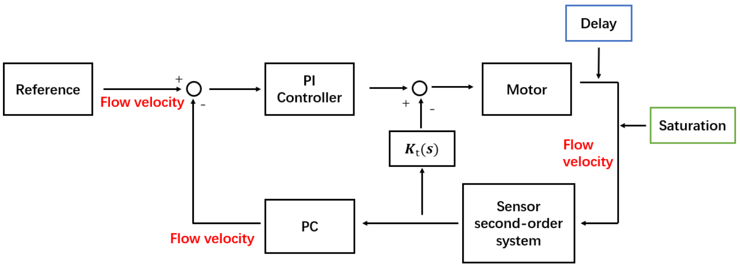

Figure 5.32: Block diagram of velocity feedback control method in Simulink.

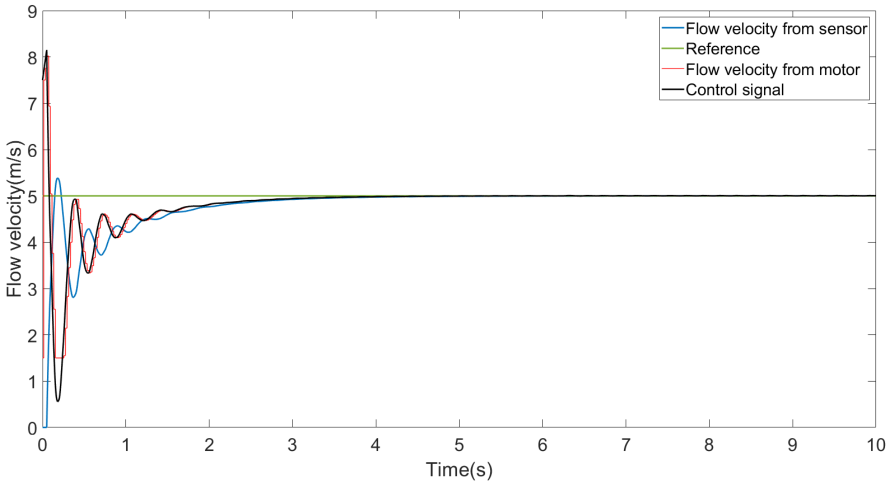

Figure 5.33: Simulation results with velocity feedback control method

It can be clearly seen from the results that the oscillation problem of the second-order system has been greatly improved, and the control system has basically stabilized after 3 s. In addition, in order to compare this control method with the low cut-off frequency method in the actual experiment, the cut-off frequency of the low-pass filter in the Simulink model is set to 0.5 Hz, and a simulation is also carried out.

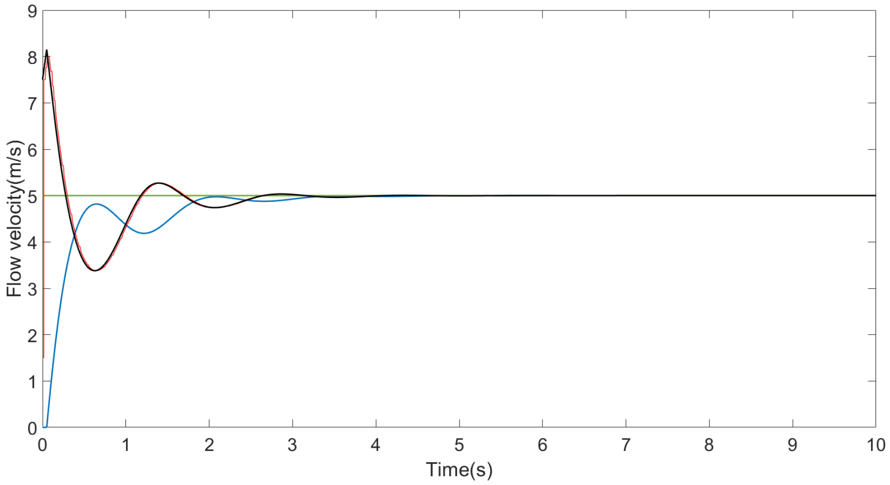

Figure 5.34: Simulation results with a cut-off frequency 0.5 Hz low pass filter

It can be seen from the vibration frequency of the signal that the low cut-off frequency method will make the system very slowly compared to the velocity feedback control method.

Overall, the problems in the experimental results of only feedback control system may come from the under-damping problem of the sensor's second-order sensor system. And velocity feedback control method can deal with this kind of problem well.

5.6.7 Conclusion of control system experiment

First, the sensor basically can not help the control system which includes a feed forward loop work. Second, the experiment of sine wave reference shows that the drift of the sensor will increase over time and affect the accuracy of the measurement. This result is consistent with the analysis of the sensor mechanical characterization experiment results. Third, the sensor shows under-damping problems in the control system of the only feedback loop, which is consistent with the analysis in the dynamic experiment. A low-pass filter with a cut-off frequency of 0.5 Hz can solve this problem. Finally, through the simulation in Simulink, the instability problem of the system may indeed come from the under-damping of the sensor's second-order system, and velocity feedback control method is proposed to better solve this problem.

5.7 Conclusion

In this chapter, the experimental results of this project have been displayed, and some preliminary analysis and discussion have been carried out. The initial experiment selected the best sensor as No. 13, the mechanical sensor characterization experiment obtained the approximate relationship between the sensor resistance change and the deformation. In addition, the wind tunnel experiment provides a more accurate and stable airflow, and further analyzes the characteristics of the sensor. The control system experiment tested the sensor's working conditions in various control loops and different references. Further discussion of these results will be carried out in the next chapter 6, and will discuss the problems that need to be solved and development prospects of this sensor.

6 Discussion and Conclusion

This chapter is the last part of the report, and it will include the discussion and conclusions of the entire project. In addition, this chapter will also give suggestions for future work.

6.1 Discussion

In this part, results and analysis from previous chapters including design, fabrication, and experiments will be discussed in more detail.

6.1.1 Design of the sensor

The design of the sensor is a very important part of this project. It directly affects the measuring range, sensitivity and stability of the sensor. In Chapters 2 and 3, various concepts and models were tried. Experimental results show that sensor 13 of model 6 has sensitive resistance changes and provides the most stable measurement signal.

Compared with other sensors, sensor 13 has a smaller connection bridge (connecting part of two strain gauges on the same surface) and bottom connection part. So, its overall resistance is smaller. In addition, its strain gauges are also the longest among all small sensors, so its resistance change values are also the largest. Based on these two points, sensor 13 has the best sensitivity.

In these designs, aerodynamic considerations are lacking, and in fact this can be considered in the future to improve the design.

6.1.2 Fabrication

The manufacturing work of the project is described in Chapter 3. However, according to the actual printing results, the thickness of the sensor cannot be too small. The strain gauges on both sides of the sensor need at least two layers to ensure that they are electrically isolated from each other.

In addition, the biggest problem in printing is that the roughness of the upper and lower surfaces of the sensor are always different, and the side close to the glass is always very smooth, even using soluble support part (pva) cannot solve this problem. The different roughness of the two surfaces is likely to cause differences in their electrical characteristics, which will bring more errors.

6.1.3 Initial experiment

In the initial experiment, a small fan is used to study the sensors response under an airflow created by the propeller. In the experimental results, it can be seen that for sensor 13 of model 6, it has two different surfaces, one of which is smoother and the other is rougher. This problem is discussed in section 6.1.2. Under the same flow velocity, the smooth side always has a larger change in resistance than the rough side. This shows that there are some differences between the two surfaces, which is inconsistent with the expectation that both sides of the sensor are exactly the same during the design. This difference will likely also cause the drift on both sides to be different. It will affect the results of calculating the flow velocity from the difference in resistance change of the two sides of the strain gauges.

In Chapter 3, for the large sensors 8 and 9, a support part is attempted to solve this problem. But from the results, even if the support part is made of this PVA material and placed between the smooth side and the glass, there is still a gap in the roughness of the two surfaces, and the resistance change characteristics between the two sides is still different.

6.1.4 Mechanical sensor characterization and dynamic test

In this part of the experiment, an approximate linear relationship between resistance and deformation is determined. However, according to the results in (Fig. 5.13), the relationship between the two is actually somewhat non-linear because of drift and hysteresis. This approximation will inevitably lead to some errors which is shown in (Fig. 5.14), thereby affecting the accuracy of the sensor for actual airflow measurements.

And for the dynamic test, the eigenfrequency of sensor is around 20 Hz and quality factor is around 10, which show that the system is an under-damping second-order system.

6.1.5 Wind tunnel experiment

From the sensor oscillations in the laminar flow in the wind tunnel, it can be known that the sensor oscillations are not caused by turbulence in the free stream or by some control. So the oscillations have to be caused by the fluid-structure interaction between the flow and the sensor. Also the wind tunnel measurements also show the drift and hysteresis in the sensor.

6.1.6 Control system experiment

In a system with feedforward auxiliary control, the sensor can not work well. Because the feedforward control signal is too stable, the entire PI controller and sensor do not play a role in feedback regulation.

For sine wave reference experiment, the measurement error can be clearly seen, and it will increase over time. This result is also consistent with the analysis in mechanical sensor characterization. This measurement error comes from the drift caused by the long-term deformation of the sensor, so it also shows that this 3D printed flow sensor is not suitable for long-term quantitative measurement work.

For a system containing only a feedback loop, the control system will become unstable due to sensor's under-damping characteristics. This situation is also consistent with the results in the dynamic experiment. A low-pass filter with a cut-off frequency of 0.5 Hz can effectively solve this problem. The result proves that the sensor can work in this PI closed-loop control system.

The simulation in Simulink later confirmed the correctness of these inferences. In the simulation, an under-damping second-order system can reproduce the problems in the experiment very well. And the simulation proves that velocity feedback control can better solve this problem.

6.2 Conclusion

According to the objectives established in Chapter 1, the following conclusions can be obtained:

- In the design part, a piezo-resistive flow sensor is designed. The best measurement range of this sensor is $2\,\mathrm{m\,s^{-1}}$-$7\,\mathrm{m\,s^{-1}}$, and the error is within $1\,\mathrm{m\,s^{-1}}$. From the calibration results, it is basically correct to calculate the relationship between deformation and flow velocity by treating the bending part of the sensor as a cantilever beam. In addition, the dynamic model of the sensor is regarded as a second-order system and basically conforms to the dynamic experimental results.

- In the 3D printing part, the designed sensor model was successfully printed and had a good quality. However, there is always some difference in roughness on both sides of the sensor. Where smooth and rough surfaces of the sensor have a different resistance.

- In the characterization part of the study, the relationship between sensor deformation and resistance change is obtained. There is a certain non-linearity and hysteresis in this relationship. Further, for the convenience of calculation, an approximate linear relationship between them is obtained: $\Delta L/L = 0.4363 \times \Delta R/R$. And in the dynamic experiment, the eigenfrequency is 20 Hz, quality factor is 10 of the sensor is obtained.

- In the wind tunnel experiment, the results show that there are some oscillations that are caused by the interaction between the sensor and the flow. Hence, the fluid-structure interaction needs to be taken into account for the future sensor design.
- In the experiment of the control system, the result shows that this kind of sensor is suitable for a PI closed-loop control system. Although, the sensor can be regarded as an under-damping second-order system, which will constantly oscillate and is difficult to stabilize in a short period of time. But, a low pass filter with a cut-off frequency=0.5 Hz or velocity feedback control method can effectively deal with this problem.

  In addition, the sensor will also produce measurement errors due to drift during long-term deformation, which indicates that this kind of flow sensor may not be suitable for long-term measurement.

In summary, this type of 3D printing flow sensor has a certain ability to measure flow velocity. And it is suitable for working in PI close-loop control system.

6.3 Future Work

Suggestions for future work mainly include the following aspects:

1. Improve the design of the sensor. The design of the sensor has a very important influence on the characteristics of this 3D printed sensor. The design should make it more sensitive under flow velocities. Several different design schemes are tried in this project, but there is still some space for improvement in this part of the work. In addition, in the design of the sensor, the influence of fluid mechanics can be considered, so that the relationship between the vibration and the airflow can be better.
2. Improve the printing method of the sensor to eliminate the difference between the two sides as much as possible. It can be seen from the experimental conclusions that the characteristics of the rough surface and the smooth surface of the sensor are somewhat different. This difference will definitely affect the resistance change characteristics of strain gauges when the sensor is deformed. For experimental accuracy, these differences need to be reduced or even eliminated.
3. More precise equipment can be used which can observe the real airflow in the experimental environment. This project uses propellers to generate airflow, but this airflow is somewhat different from constant airflow. And in the experiment, the actual airflow generated by the propeller is calculated from the data of the motor encoder, which lacks the detection of the real airflow around the sensor. Therefore, the use of wind tunnels or other more precise equipment is a huge improvement to this project. If real-time information of the airflow around the sensor can be seen, the dynamic analysis of the sensor during the experiment will be more accurate.
4. Improve the strategy of the control system, and solve the problem of sensor's under-damping. In this report, a low pass filter with a small cut-off frequency is a good solution, but it will make the system very slow. And, velocity feedback control shows a good performance in simulation, but it also still needs experimental validation.

A MATLAB Code

This part will show some important MATLAB code in this project.

A.1 SMAC position change code

```
 function smacTest(tend)

% Initiate connection
actuator = SMAC_init(3);

% Define parameters
t = zeros;                  % starting time
f = 0.5;                    % excitation frequency
t_i = 1;
t(1) = 0;
i1 = 1;
offset = 50;
amplitude = 600;
lamda = 0.015; % decaying constant (lower value-slows decay rate)

% Account for data reading start delay
t_offset = 0; % sec
tend = tend + t_offset;

% frequency sweep parameterers
f1 = 0.005; %Hz
f2 = 3; %Hz
ratio = f2/f1;

% Command loop
tic
while t(end) < tend
    if t(end) > t_offset
        time(i1) = posixtime(datetime('now')) * 1e6;
        % sinusoid
        x = offset+amplitude*sin(2*3.14*f*t(end));
        % decaying sinusoid
%           x = offset+amplitude*exp(-lamda*t(end))*(cos(2*3.14*f*t(
    end))+sin(2*3.14*f*t(end)));
        % sinusoid frequency sweep
%           x = offset+amplitude*sin(2*3.14*tend*((ratio^(t(end)/tend
    )-1)/log(ratio))); % exponential
%           x = offset+amplitude*cos(2*3.14*(f1+((f2-f1)/tend)*t(end)
    )*t(end)); % linear
        [position(i1),force(i1)] = SMAC_read_and_set_Position(
            actuator,x);
    end
    t(i1) = toc;
    i1=i1+1;
```

```
end % end while

% set position to center for next measurment and sensor "relaxation"
SMAC_read_and_set_Position(actuator,offset);

% Uncomment if actuator command data are required
%save(['data_log\SMAC\distance',mat2str(counter), '.mat'],'position','force','time');

% Terminate connection
fclose(actuator);

end % end function
```

A.2 Sensor mechanical characterization stream code

```
clear all
close all

addpath('hs5_drivers')

import LibTiePie.Const.*
import LibTiePie.Enum.*

system = HS5_CPU();
system.gen_offset = [2, 2] % voltage
system.gen_type = [ST.DC, ST.DC];

system.scope_ranges = [12,12,12,12];
system.scope_couplings = [CK.DCV, CK.DCV, CK.DCV, CK.DCV];
system.scope_block_size = 625e3;
system.scope_fs = 6.25e6; %sampling frequency (Hz)

tend = 30; % experiment time (seconds)
downsample_ratio = 50; % on-measurement downsampling
filename = 'data.mat';

k = length(system.scope_ranges);
n = ceil(tend*system.scope_fs/system.scope_block_size);

block_size_downsampled = system.scope_block_size/downsample_ratio;
fs_downsampled = system.scope_fs/downsample_ratio;

%q = HS5_streaming_start(n,fs, ranges,couplings,block_size);
system = start_streaming_with_gen(system,n);

tic

data = zeros((n-1)*block_size_downsampled,k,'single');
t = zeros((n-1)*block_size_downsampled,1);
```

```
disp('Measurement start!')
for i1 = 1:n-1
    [system,newData,new_t]=get_data_downsampled(system,
        downsample_ratio,i1);
    loc=(i1-1)*block_size_downsampled+1:i1*block_size_downsampled;
    data(loc,:) = newData;
    t(loc) = new_t;

    %loc(1)
    %loc(end)
%      i1
end
toc
disp('finished measuring')

% save data
filepath = ['../post_process/data/' filename];
save(filepath, 'data','t', '-v7.3','-nocompression');

% plot data
plot_data(data,system.scope_fs,downsample_ratio)
```

A.3 Sensor mechanical characterization post process code

```
% post-processing of data

%load data
filename = 'data';
datafile = ['data/' filename];
load(datafile)

% scope settings
fs = 6.25e6;
downsampling_ratio = 50;

% extract sensor data

sensor1 = data(:,1);
sensor2 = data(:,2);

% extract encoder data
encA = data(:,3);
encB = data(:,4);

% get time-step
fs_ds = fs/downsampling_ratio;
dt = 1/fs_ds;

% obtain time vector from time step
t = zeros(length(sensor1),1);
```

```
for i1 = 2:length(sensor1)
    t(i1) = t(i1-1)+dt;
end

% set tolerance for encoder FSM
tol = 0.2;

% get position from encoder pulses
encoder_position = encoder2(encA,encB,tol);

% plot SMAC position
figure(3)
plot(t,encoder_position)
```

A.4 Drone propeller control code

```
%% CCC
close all
clear
clc

%% genom
username='youssef';

% Put the custom path that you used for the ROBOTPKG_BASE
ROBOTPKG_BASE = strcat('/home/', username, '/openrobots/');
devel_path = strcat(ROBOTPKG_BASE, 'lib/genom/pocolibs/plugins/');

addpath(strcat(ROBOTPKG_BASE,'lib/matlab'));
addpath(strcat(ROBOTPKG_BASE,'lib/matlab/simulink'));
addpath(strcat(ROBOTPKG_BASE,'lib/matlab/simulink/genomix'));

host = 'localhost';
client = genomix.client(host);
%% Parameters

% FC board Sensor Rate
s_rate_imu = 50;
s_rate_mag = 1;
s_rate_motor = 50;
s_rate_battery = 1;

m_max_speed = 100;
m_min_speed = 20;



%% Init rotorcraft genom component

disp('* Initialize Mikrocopter');
rotorcraft = client.load(strcat(strcat(devel_path,'rotorcraft')));
```

```
pause(1);

% connect
result_mk = rotorcraft.connect('/dev/ttyUSB0', 500000);
stringmsg = ['Connecting to mikrokopter: ',result_mk.status];
disp(stringmsg);

rotorcraft.set_sensor_rate(s_rate_imu, s_rate_mag, s_rate_motor,
    s_rate_battery );


%% start motors
rotorcraft.start('-a');

%% start log
rotorcraft.log('/tmp/rotor.log',1)

%% main

% speed cmd profile
mot_cmd = 30*ones(1,10000);

% init data size
omega_hz        = zeros(1,length(mot_cmd));
throttle_perc   = zeros(1,length(mot_cmd));
current_a       = zeros(1,length(mot_cmd));
enenrgy_lvl     = zeros(1,length(mot_cmd));
mot_ts_sec      = zeros(1,length(mot_cmd));
mot_ts_nsec     = zeros(1,length(mot_cmd));


for i=1:1:10000

 rotorcraft.set_velocity({0, 0, mot_cmd(i), 0, 0, 0, 0, 0});

rotormeasure = rotorcraft.rotor_measure();

 omega_hz(i)       = rotormeasure.rotor_measure.rotor{3}.velocity;
 throttle_perc(i)  = rotormeasure.rotor_measure.rotor{3}.throttle;
 current_a(i)      = rotormeasure.rotor_measure.rotor{3}.consumption
     ;
 enenrgy_lvl(i)    = rotormeasure.rotor_measure.rotor{3}.
     energy_level;

 mot_ts_sec(i)     = rotormeasure.rotor_measure.rotor{3}.ts.sec;
 mot_ts_nsec(i)    = rotormeasure.rotor_measure.rotor{3}.ts.nsec;


end
%%
rotorcraft.stop('-a');
```

```
%%
rotor.log_stop()
```

A.5 Wind tunnel experiment data process code

```
close all;

v0_1=getsampleusingtime(flowvelocity,0,10);
v2_1=getsampleusingtime(flowvelocity,10,20);
v4_1=getsampleusingtime(flowvelocity,20,30);
v6_1=getsampleusingtime(flowvelocity,30,40);
v8_1=getsampleusingtime(flowvelocity,40,50);
v10=getsampleusingtime(flowvelocity,50,60);
v8_2=getsampleusingtime(flowvelocity,60,70);
v6_2=getsampleusingtime(flowvelocity,70,80);
v4_2=getsampleusingtime(flowvelocity,80,90);
v2_2=getsampleusingtime(flowvelocity,90,100);
v0_2=getsampleusingtime(flowvelocity,100,110);
%0m/s first time
v0_1t=v0_1.Time;
v0_1d=v0_1.Data;

v0_1data=zeros(501,1)
for i=1:1:501;
    v0_1data(i,1)=v0_1d(:,:,i);
end

v0_1a=mean(v0_1data,1)
v0_1e=std(v0_1data)

figure
errorbar(0,v0_1a,v0_1e,'xr')
hold on
%2m/s first time
v2_1t=v2_1.Time;
v2_1d=v2_1.Data;

v2_1data=zeros(501,1)
for i=1:1:501;
    v2_1data(i,1)=v2_1d(:,:,i);
end

v2_1a=mean(v2_1data,1)
v2_1e=std(v2_1data)

errorbar(2,v2_1a,v2_1e,'xr')
hold on
%4m/s first time
v4_1t=v4_1.Time;
v4_1d=v4_1.Data;
```

```
v4_1data=zeros(501,1)
for i=1:1:501;
    v4_1data(i,1)=v4_1d(:,:,i);
end

v4_1a=mean(v4_1data,1)
v4_1e=std(v4_1data)

errorbar(4,v4_1a,v4_1e,'xr')
hold on
%6m/s first time
v6_1t=v6_1.Time;
v6_1d=v6_1.Data;

v6_1data=zeros(501,1)
for i=1:1:501;
    v6_1data(i,1)=v6_1d(:,:,i);
end

v6_1a=mean(v6_1data,1)
v6_1e=std(v6_1data)

errorbar(6,v6_1a,v6_1e,'xr')
hold on
%8m/s first time
v8_1t=v8_1.Time;
v8_1d=v8_1.Data;

v8_1data=zeros(501,1)
for i=1:1:501;
    v8_1data(i,1)=v8_1d(:,:,i);
end

v8_1a=mean(v8_1data,1)
v8_1e=std(v8_1data)

errorbar(8,v8_1a,v8_1e,'xr')
hold on
%10m/s
v10t=v10.Time;
v10d=v10.Data;

v10data=zeros(501,1)
for i=1:1:501;
    v10data(i,1)=v10d(:,:,i);
end

v10a=mean(v10data,1)
v10e=std(v10data)
```

```
errorbar(10,v10a,v10e,'xr')
hold on
%8m/s second time
v8_2t=v8_2.Time;
v8_2d=v8_2.Data;

v8_2data=zeros(501,1)
for i=1:1:501;
    v8_2data(i,1)=v8_2d(:,:,i);
end

v8_2a=mean(v8_2data,1)
v8_2e=std(v8_2data)

errorbar(8,v8_2a,v8_2e,'xb')
hold on
%6m/s second time
v6_2t=v6_2.Time;
v6_2d=v6_2.Data;

v6_2data=zeros(501,1)
for i=1:1:501;
    v6_2data(i,1)=v6_2d(:,:,i);
end

v6_2a=mean(v6_2data,1)
v6_2e=std(v6_2data)

errorbar(6,v6_2a,v6_2e,'xb')
hold on
%4m/s second time
v4_2t=v4_2.Time;
v4_2d=v4_2.Data;

v4_2data=zeros(501,1)
for i=1:1:501;
    v4_2data(i,1)=v4_2d(:,:,i);
end

v4_2a=mean(v4_2data,1)
v4_2e=std(v4_2data)

errorbar(4,v4_2a,v4_2e,'xb')
hold on
%2m/s second time
v2_2t=v4_2.Time;
v2_2d=v4_2.Data;

v2_2data=zeros(501,1)
for i=1:1:501;
    v2_2data(i,1)=v2_2d(:,:,i);
```

```
end

v2_2a=mean(v2_2data,1)
v2_2e=std(v2_2data)

errorbar(2,v2_2a,v2_2e,'xb')
hold on
%0m/s second time
v0_2t=v0_2.Time;
v0_2d=v0_2.Data;

v0_2data=zeros(501,1)
for i=1:1:501;
    v0_2data(i,1)=v0_2d(:,:,i);
end

v0_2a=mean(v0_2data,1)
v0_2e=std(v0_2data)

errorbar(0,v0_2a,v0_2e,'xb')
hold on;
```

Bibliography

[1] M. Schouten, B. Prakken, R. Sanders, and G. Krijnen, "Linearisation of a 3d printed flexible tactile sensor based on piezoresistive sensing," in *2019 IEEE Sensors*, (United States), IEEE, Jan. 2020. 2019 IEEE SENSORS ; Conference date: 27-10-2019 Through 30-10-2019.

[2] D. Kosmas, M. Schouten, and G. Krijnen, "Hysteresis compensation of 3d printed sensors by a power law model with reduced parameters," in *2020 IEEE International Conference on Flexible and Printable Sensors and Systems (FLEPS)*, pp. 1–4, 2020.

[3] A. Dijkshoorn, P. Werkman, M. Welleweerd, G. Wolterink, B. Eijking, J. Delamare, R. Sanders, and G. Krijnen, "Embedded sensing: Integrating sensors in 3-d printed structures," *Journal of Sensors and Sensor Systems*, vol. 7, pp. 169–181, 2018.

[4] B. Eijking, R. Sanders, and G. Krijnen, "Development of whisker inspired 3d multi-material printed flexible tactile sensors," in *IEEE SENSORS 2017*, (United States), IEEE, Dec. 2017. 16th IEEE Sensors 2017 ; Conference date: 29-10-2017 Through 01-11-2017.

[5] W. Su and G. W. Reich, "Geometric scaling of artificial hair sensors for flow measurement under different conditions," *Smart Materials and Structures*, vol. 26, p. 037002, feb 2017.

[6] M. Schouten, "Towards additively manufactured complex robotic systems," December 2017.

[7] NinjaTek, "Ninjaflex 85 a."

`https://ninjatek.com/ninjaflex`.

[8] E. ToolBox, "Cantilever beams - moments and deflections."

`https://www.engineeringtoolbox.com/cantilever-beams-d_1848.html`.

[9] NinjaTek, "Young's modulus ninjaflex."

`https://ninjatek.fppsites.com/wp-content/uploads/2018/10/tech-data-metric.pdf`.

[10] IPFS, "Density of air."

`https://ipfs.io/ipfs/QmXoypizjW3WknFiJnKLwHCnL72vedxjQkDDP1mXWo6uco/wiki/Density_of_air.html#cite_note-SInote01-13`.

[11] NASA, "Shape effects on drag."

`https://www.grc.nasa.gov/WWW/k-12/airplane/shaped.html`.

[12] L. Howell and A. Midha, "A method for the design of compliant mechanisms with small-length flexural pivots," *Journal of Mechanical Design*, vol. 116, pp. 280–290, 1994.

[13] Wikipedia, "Torsion spring."

`https://en.wikipedia.org/wiki/Torsion_spring`.

[14] A. Aly, "Velocity feedback control of a mechatronics system," *International Journal of Intelligent Systems and Applications*, vol. 5, 07 2013.

[15] DIABASE, "Diabase h-series multi-material 3d printer."

`https://www.diabasemachines.com/`.

[16] eSUN, “esun3d.net..”

`http://www.esun3d.net/products/82.html`.

[17] S. S. Roodink, “Controlling deformations of a 3d-printed vibrating beam using stiffness modulation,” 2020.

[18] ARDUINO, “Arduino uno rev3.”

`https://store.arduino.cc/arduino-uno-rev3`.

[19] DFRobot, “Gravity I2C ADS1115 16-Bit ADC Module Arduino.”

`https://wiki.dfrobot.com/Gravity__I2C_ADS1115_16-Bit_ADC_Module_Arduino_26_Raspberry_Pi_Compatible__SKU__DFR0553`.

[20] A. T. E. Corporation, “Mb dynamics pm50a shaker.”

`https://www.atecorp.com/products/mb-dynamics/pm50a`.

[21] AEROLAB, “AEROLAB Educational Wind Tunnel.”

`https://www.aerolab.com/products/educational-wind-tunnel-ewt`.

[22] NASA, “Propeller analysis.”

`https://www.grc.nasa.gov/www/k-12/airplane/propanl.html`.

[23] K. Rawson and E. Tupper, “10 - powering of ships: general principles,” in *Basic Ship Theory (Fifth Edition)* (K. Rawson and E. Tupper, eds.), pp. 365–410, Oxford: Butterworth-Heinemann, fifth edition ed., 2001.

[24] bitfab, “The densities of all 3d printing materials.”

`https://bitfab.io/blog/3d-printing-materials-densities/`.

[25] Tutorialspoint, “Response of second order system.”

`https://www.tutorialspoint.com/control_systems/control_systems_response_second_order.htm`.

[26] M. Païdoussis, S. Price, and E. de Langre, *Fluid-Structure Interactions: Cross-Flow-Induced Instabilities.* Cambridge University Press, 2010.